**RESEARCH**

# Advanced, universal, and facile gel spinning-based aerogel fibrillation: in situ fabrication of highly stretchable TPU-silica hybrid network in ambient conditions

Hosseinali Omranpour[1] · Soran Hassanifard[2] · Ali Reza Monfared[1] · Babak O. Shahreza[3,4,5] · Amirmehdi Salehi[1] · Amirjalal Jalali[1] · Mohamad Kheradmandkeymousi[1] · Saadman Sakib Rahman[1] · Kamran Behdinan[2] · Chul B. Park[1]

## Abstract

Innovations in synthesis and processing are critical for making high-performance aerogel fibers. Here, we present a novel method for creating highly stretchable aerogel fibers with exceptional thermal insulation. This innovative approach involves flow-assisted orientation and a dual-crosslinking strategy within a gel spinning system, all achievable in ambient conditions. Trimethoxy silane propyl isocyanate (TEPI) was grafted onto thermoplastic polyurethane (TPU) to create TPU-g-TEPI. This modified TPU (mTPU) is then dissolved in dioxane at varying concentrations while incorporating finely ground silica aerogel (SA) as a thickening agent. Rheological analysis confirms the formation of a physically entangled network of TPU and SA particles, displaying a significant increase in viscosity and yield stress. The resulting crosslinked hybrid network demonstrates thermal and mechanical robustness, with a highly porous structure, hierarchical morphology, and improved thermal stability. The mesoporous nature of the silica aerogel significantly reduces thermal conductivity to $0.024\ \mathrm{W \cdot m^{-1} \cdot k^{-1}}$ and enhances thermal stability up to 400 °C. While crosslinked TPU nanofibers exhibit tensile stress and strain of 10.26 MPa and 100.94%, respectively, these mechanical properties remained stable over a broad temperature range from −60 to 150 °C. This study also offers fundamental insights into the currently unknown fatigue behavior of aerogel fibers, serving as a starting point for dynamic reliability evaluations. The versatile gel spinning technique holds great promise for revolutionizing high-performance aerogel fiber production. These advanced fibers hold significant prospects for diverse applications, including protective clothing and stretchable apparel, particularly in harsh environments.

**Keywords** Aerogel fibers · In situ nanofibrillation · Gel spinning · Protective clothes · Stretchable network

## Highlights

- Novel gel-spinning technique created nanofibers in the fiber structure.
- Dual-crosslinking of silica aerogel (SA) and thermoplastic polyurethane (TPU) yields flexible and robust integrity.
- Resultant aerogel fibers show outstanding dynamic reliability.
- Inclusion of TPU nanofibers whitin SA particles significantly improves stretchability.

✉ Chul B. Park
park@mie.utoronto.ca

1 Microcellular Plastics Manufacturing Laboratory, Department of Mechanical and Industrial Engineering, University of Toronto, Toronto, ON M5S 3G8, Canada

2 Advanced Research Laboratory for Multifunctional Lightweight Structures (ARL-MLS), Department of Mechanical and Industrial Engineering, University of Toronto, Toronto, ON M5S 3G8, Canada

3 Hydrogen Research Institute, University of Quebec in Trois-Rivieres (UQTR), 3351 des Forges, Trois-Rivieres, QC G9A 5H7, Canada

4 Department of Mechanical and Industrial Engineering, Tallinn University of Technology (TalTech), Ehitajate tee 5, Tallinn 19086, Estonia

5 Department of Chemical and Materials Engineering, Complutense University of Madrid (UCM), Av. Complutense, Madrid 28040, Spain

## 1 Introduction

Fibrous materials are widely employed in protective clothing industry where advancements aimed at achieving specific characteristics, and performance for targeted applications is bringing a new era of innovation and materialization [1–3]. Due to their unique structure, fibrous materials possess

inherently high thermal insulation properties, making them a preferred choice to meet the thermal management demands for a wide variety of applications [4–8]. Nonetheless, traditional thermal management solutions employing natural or synthetic fibers often fall short in addressing the requirements for complex applications, such as thermal insulation in extreme environments or the provision of comfort alongside thermal protection [9].

Recent advancements in synthetic fibers, including hollow fibers, biomimetic porous fibers, and ultrafine fibers, have shown promise in terms of heat insulation. However, there is still a demand for the design of super thermal insulating fibers with even more efficient thermal insulation properties. Although numerous thermally insulating fibrous materials have been employed to date, their limitations in heat resistance and thermal insulation effectiveness render them inadequate for extreme environmental conditions [10–12]. Not to mention, extreme cold can render conventional clothing brittle, necessitating a highly stretchable fabric composition to ensure flexibility even in harsh conditions. To overcome these challenges, aerogel fibers are the prime contender.

High-performance aerogel fibers offer potential applications in various sectors, particularly in textiles like firefighter clothing and personal thermal management. These innovative materials are substantially lighter than existing fibers, capable of enhancing the performance of thermal management fabrics [13]. These fibers offer the dual advantages of low density and high specific strength, and they can be processed into complex shapes akin to other fibers, due to their small diameters, which minimize structural defects [13]. Moreover, transitioning from a brittle bulk material to a 2D film and eventually to a 1D fiber has been demonstrated to enhance mechanical performance, as observed in glass [14–17]. However, the highly porous structure and fractal necklace-like network of aerogels can compromise mechanical strength [18, 19]. Solvent removal disrupts the structure and properties of aerogel fibers, acts as stress concentration points, and eventually weakens tensile strength [13]. Multiple efforts have been made so far to enhance the mechanical properties of aerogel fibers, either through the inclusion of polymeric materials [20, 21] or the incorporation of nanostructure materials [22, 23]. Numerous studies have primarily focused on material type, with only a few examining critical factors such as thermodynamics of fibrillation, crystallization, and in situ nanofibrillation [24, 25].

The innovative technique of in situ nanofibrillation allows for the creation of rubbery nanofibrils within high-performance aerogel fibers, featuring intricate geometries and exceptional mechanical properties not easily attainable with traditional processing methods. This method involves the stretching or fibrillation of an immiscible blend of two or more polymers, where the resulting structure, identified as a fiber-in-fiber geometry, is composed of nanofibrils of the minor phase oriented in the stretch direction within the outer microfibers of the matrix phase [26]. Owing to their enhanced alignment and orientation, in situ nanofibrillated rubbers can impart superior mechanical characteristics to the aerogel fibers. This effect is much more pronounced at higher viscosities where orientation is more effective due to the negligible relaxation of molecules. Similarly, maximizing the number of covalently bonded atoms per unit volume or mass can boost fiber strength and stiffness, as the fixation of molecules inhibits the recoiling process of polymeric molecules [27, 28].

Silica aerogels (SA), renowned for their unique and exceptional features outlined in prior studies [29–31], serve as ideal building blocks for aerogel fiber production. Incorporating a polymeric phase or nanofibers into silica aerogels aids in preventing defects and brittleness by improving chain entanglement, alignment, and packing [13, 27, 28, 32]. Polymer nanofibers demonstrate superior properties when compared to their macroscopic counterparts [33]. However, it is crucial to develop fibers that are both environmentally friendly and comfortable to wear [9].

Thermoplastic polyurethane (TPU) stands out as a widely used thermoplastic elastomer with exceptional performance characteristics in various extensive conditions [26]. It boasts resistance to abrasion, excellent bending and tensile strength, substantial elongation at break, low-temperature resistance, and resistance to chemicals [34]. TPU is environmentally friendly, biodegradable, and fully recyclable. Porous TPU products contribute to material efficiency and lightweight construction, which is of paramount importance for reducing energy consumption and carbon emissions. Furthermore, the porous structure enhances TPU's mechanical properties, providing it with improved flexibility, elasticity, and cushioning capabilities. Moreover, the gas phase within the porous structure enhances TPU's insulating properties, making it suitable for applications involving heat, sound, electricity, and electromagnetic wave insulation [35, 36].

In this study, we successfully developed a straightforward approach for fabricating continuous TPU-SA hybrid aerogel fibers using a flow-assisted dual-crosslinking gel spinning strategy. Our research investigated the gel spinning method to control the thermodynamics of fibrillation and to enhance the mechanical properties through phase separation and stress-induced nanofibrillation, all while preserving favorable thermal characteristics. In situ nanofibrillation was used to generate nanofibrous mTPU structures within aerogel fibers at room temperature. By adjusting the mTPU and SA concentrations and the processing parameters, we were able to customize spinnability and in turn, the final characteristics. Then, via regulating the nozzle, the collecting rate, and the extrusion rate, aerogel fibers with adjustable diameters and tunable properties were obtained. The dual-crosslinking

strategy resulted in robust and aligned regenerated fibers with exceptional thermal insulation, thermal stability, and mechanical resilience. In this developed strategy, SA particles with high surface area absorb solvents, improving dope strength and spinnability. Simultaneously, mTPU nanofibers were connected to nearby SA particles, creating a robust aerogel with enhanced stretchability. The continuous mTPU nanofibers provided superior mechanical strength, while the porous crosslinked silica aerogel ensured outstanding thermal stability and thermal insulation performance for the final aerogel fibers. A fundamental study of fatigue behavior validated the role of flexible mTPU in enhancing fatigue resistance. The 3D network structure of mTPU embedded within the aerogel matrix minimized stress concentration sites, leading to prolonged dynamic reliability. Therefore, this study not only introduces a continuous and economically viable production method for aerogel fibers but also offers valuable insights into fatigue behavior, contributing to the dynamic reliability assessment of other aerogel fibers.

## 2 Materials and methods

### 2.1 Materials

The materials used in this study, including polymethylhydrosiloxane (PMHS, average molecular weight of 1700–3200), vinyltrimethoxysilane (VTMS, purity of 98%), tetrahydrofuran (THF, purity of 99.9%), 1,4-dioxane (dioxane, purity of 99.75%), N,N-dimethylformamide (DMF, purity of 99.75%), a platinum(0)-1,3-divinyl-1,1,3,3-tetramethyldisiloxane complex solution (containing 2% platinum in xylene), 3-(triethoxysilyl) propyl isocyanate (TEPI, purity of 94.5%), and dibutyltin dilaurate (DBTDL, purity of 95%), were all sourced from Sigma Aldrich (MilliporeSigma Canada Ltd). Anhydrous ethanol (purity of 99.5%), nitric acid (purity of 63%), and distilled water were purchased from GreenField Global, Caledon Laboratory Chemicals, and Gibco, respectively. Ether-type TPU Elastollan 1180 A10 was provided by BASF. A 2 M nitric acid solution was prepared by diluting the purchased nitric acid with distilled water. All other materials were used as received without any further purification.

### 2.2 Component preparation procedure

To create the SA constituent, as detailed in our prior work [31], we combined 148 g of VTMS with 65 g of PMHS and introduced three droplets of Pt catalyst into the solution to synthesize the silica aerogel precursor. All reactions were conducted in a 3-neck flask under a nitrogen gas atmosphere, utilizing a magnet-stirring hot plate setup equipped with a distillation column. Upon completing the reactions, we subjected the samples to degassing in a vacuum oven at 40 °C under a pressure of 25 in of mercury (Hg) to eliminate any residual monomers and achieve monomer-free precursors. Bulk aerogel specimens were prepared by dissolving 1 g of the precursor in 8 cc of anhydrous ethanol, followed by the addition of 1 cc of 2 M nitric acid. The mixture was vigorously agitated using a vortex mixer and left undisturbed until gelation occurred. Subsequently, 10 cc of ethanol was added to the surface of the specimens, and the containers were sealed tightly with lids. The samples underwent three additional ethanol rinses, each conducted at 24-h intervals. Finally, the samples were dried under supercritical $CO_2$ conditions at 1500 psi and 40 °C. The fabrication process and the ultimate structure of the prepared aerogels are depicted schematically in Fig. 1a.

As shown in Fig. 1b, Fig. S1, and discussed in our recent paper [26], following the 4-h drying of TPU pellets in a vacuum oven at 100 °C, we proceeded to create a masterbatch of 90/10 TPU-TEPI using a co-rotational twin-screw extruder (TSE, Leistritz 27 mm, L/D = 40). This involved the use of 0.2 wt% DBTDL as a catalyst, running the extruder at 100 RPM, and maintaining a temperature of 160 °C to facilitate the grafting of TEPI molecules onto the TPU chains. Subsequently, the resulting masterbatch, known as TPU-g-TEPI (mTPU), was dissolved in pure dioxane to achieve concentrations of 50, 100, 150, and 200 g·l$^{-1}$. Dioxane and mTPU were mixed in a 3-neck vessel positioned on top of a heating magnet stirrer. The mTPU pellets were carefully dispersed in dioxane at ambient temperature. At this lower temperature, the solvent's solvating power was reduced, preventing the particles from sticking together and allowing for effective dispersion. Once proper dispersion was achieved, the temperature was gradually increased to 50 °C to create a homogeneous solution. As the temperature increased, the pellets softened and fully dissolved in dioxane, resulting in the formation of highly viscous solutions.

Aerogel particles were then crushed using a laboratory grinder and subsequently combined with mTPU solutions through wet-mixing under ambient conditions to create the desired samples outlined in Table S1. In the sample names, T, S, and the accompanying digits indicate mTPU, silica aerogel powder, and their concentrations in the solution (grams per liter), respectively. For instance, T150-S75 represents the specimen with 150 g·l$^{-1}$ mTPU and 75 g·l$^{-1}$ silica aerogel. The components were blended to form a suitable paste for fibrillation, often referred to as a dope. After initial mixing with a spoon, the mixtures were vigorously agitated using a vortex mixer and then subjected to centrifugation to eliminate any trapped air and bubbles from the dope.

### 2.3 Fibrillation procedure

Alcogel filaments were spun using the experimental setup depicted in Fig. 1c. The prepared pastes were loaded into
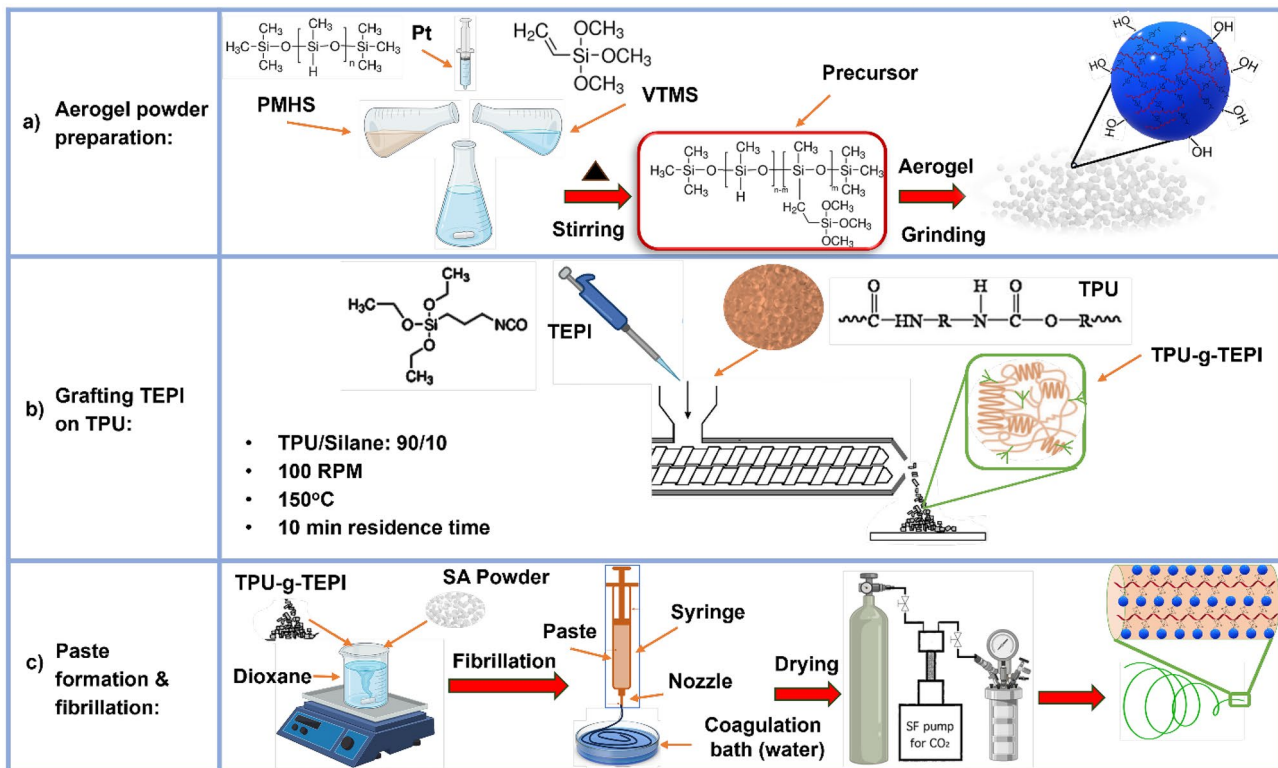
**Fig. 1** Schematic representation of synthesis, modification, and fabrication methods used in this study for developing the TPU-SA aerogel fibers. **a** Grafting VTMS on PMHS and preparing aerogel powders. **b** Grafting process of TEPI on TPU chains. **c** Paste preparation and fibrillation process of aerogel fibers

10-cc syringes equipped with 18G nozzles. To ensure a consistent rate of injection (ROI) and achieve the desired filament size, the fibrillation process was carried out with the aid of a metering pump. The metering pump pushed the gel-like paste through the nozzle, subjecting it to high pressure, resulting in the formation of slender filaments in a coagulation bath. The highly viscous, gel-like phase was continuously pumped and underwent coagulation in a cold-water bath containing 0.1 M nitric acid to complete the crosslinking reactions. The as-spun filaments, emerging from the nozzle, precipitated and solidified in the coagulation bath, giving rise to the gel fibers. Subsequently, a chemical reaction between the silane sites on both constituents took place, preserving the structure of these continuous gel filaments. The system was equipped with a rotating coagulation bath to control the rate of collection (ROC) and, consequently, the final diameter of the fibers. Using this technique, hybrid pastes were transformed into elastic alcogel fibers. After spinning, the fibers were left in the coagulation bath for 2 h to promote the development of the mTPU-SA structure through silane-grafted sites, as shown in Fig. S2. The alcogel fibers were then soaked, aged, and washed in ethanol for 24 h to remove all catalysts, solvents, and residual water. These specimens were subsequently dried using supercritical $CO_2$ conditions at 1500 psi and 40 °C to yield aerogel fibers.

## 2.4 Characterization

Rheological properties of the samples were assessed using a controlled strain rheometer (ARES, TA Instruments, New Castle, DE), featuring a parallel plate geometry with a diameter of 25 mm and a gap height of 0.5 mm. This geometry was consistently employed for all rheological experiments. Prior to testing, the aerogel pastes were allowed to equilibrate for 1 min. Rheological measurements were executed in the shear-rate mode of the motor, employing steady-state flow experiments with a range of shear rates from 0.01 to 10 s$^{-1}$. Through oscillation experiments at a fixed frequency of 1 Hz, we determined apparent viscosities, storage modulus, loss modulus, and phase angle ($\delta$) as functions of shear stress. Small amplitude oscillatory shear (SAOS) measurements were also conducted within the linear viscoelastic strain region. These oscillatory measurements allowed us to obtain the elastic modulus (G′), loss modulus (G″), and complex viscosity within the linear viscoelastic range, as validated by strain sweeps on all solutions and gels. These assessments were conducted at a 1% strain within a

frequency range of 0.1–628 Hz at 25 °C, and each measurement was performed in triplicate at a minimum.

We employed a Fourier transform infrared (FTIR) spectrometer (Bruker Platinum-ATR) to explore functional group alterations in specimens within the range of 500–4000 cm$^{-1}$. The apparent density was determined by weighing samples with known dimensions. Proton nuclear magnetic resonance ($^1$H NMR) spectroscopy was conducted to discern the structural characteristics of the components. $^1$H NMR spectra were acquired using an Agilent DD2 500MHZ instrument with chloroform (CDCl$_3$) as the solvent.

For longitudinal and cross-sectional morphology observations, a field emission scanning electron microscope (FESEM, Hitachi S-5200) operating at an acceleration voltage of 5–15 kV was used. The samples were cryogenically fractured by immersing them in liquid nitrogen, and then the surfaces were coated with a thin layer of carbon for improved conductivity.

Nitrogen adsorption-desorption isotherm analysis was conducted using an Autosorb IQ instrument from Quantachrome, USA. The pore size and pore size distribution (PSD) were examined using density functional theory (DFT) analysis of the nitrogen adsorption branch. Prior to each measurement, the samples underwent degassing under vacuum at 40 °C for 16 h.

To measure the static contact angles of the samples, we employed the OCA 15EC instrument. The sessile drop method was utilized, involving the careful placement of a small volume of liquid (ranging from 1 to 5 μL) on the smooth surface of the sample using a single direct dosing system. The process was recorded using a high-speed camera to capture the image of the droplet on the surface, enabling accurate determination of the static contact angle.

To analyze the thermal behavior of the samples, we utilized differential scanning calorimeter (DSC Q2000, TA Instruments), thermogravimetry analysis (TGA), and dynamic mechanical analysis (DMA). For DSC tests, the samples were maintained within a weight range of 4–5 mg and were initially heated to 210 °C and subsequently cooled to −70 °C at a rate of 10 °C·min$^{-1}$. Thermogravimetric analysis curves were recorded in a simultaneous thermal analyzer (NETZSCH STA 449 F3 Jupiter) under an N$_2$ atmosphere, involving a thermal ramp from room temperature to 800 °C at a rate of 10 °C·min$^{-1}$. DMA was conducted in a TA instrument Q800 with a heating rate of 3 °C·min$^{-1}$ in tension mode and a temperature range from −60 to 180 °C. The force track, frequency, and strain were set to 150%, 1 Hz, and 0.25%, respectively.

The mechanical properties of these monofilaments were evaluated at room temperature using an Instron 5965. Varying the testing speed from 5 to 300 mm·min$^{-1}$ did not impact the stress-strain behavior. Consequently, all samples, with an initial length of 8 cm, were tested at a cross-head speed of 50 mm·min$^{-1}$. Before testing, the samples were stored at room temperature for 48 h to ensure equilibrium. To ensure statistical significance, at least three replicate samples were tested in each category, and the mean values, along with the corresponding standard deviations, were calculated. Furthermore, the fatigue behavior of the aerogels was also investigated to assess their long-term flexibility in practical applications.

Thermal conductivity measurements were implemented at room temperature using Hot Disk TPS 2500 S (Thermtest Inc.) and Kapton sensor C7577. XRD patterns were acquired employing a Phillips PW3710 X-ray diffractometer, with diffraction angles (2$\theta$) analyzed in the range of 5–60° at a scanning rate of 0.04°·min$^{-1}$.

Small-angle X-ray scattering (SAXS) and wide-angle X-ray scattering (WAXS) measurements were performed using a SAXSpoint 2.0 instrument (Anton Paar, Austria) equipped with a Cu Kα radiation source ($\lambda = 1.54$ Å) and an Eiger R 1 M (Horizontal) detector, with SAXS and WAXS distances of 1075.9 mm and 113.1 mm, respectively. The SAXS profiles were background-corrected and presented as a function of the scattering vector $q = (4\pi/\lambda) \sin\theta$, where $\theta$ represents the scattering angle. One-dimensional (1D) SAXS plots were generated by integrating the intensity over azimuthal angles ranging from 0° to 360°. The determination of long periods was carried out through correlation function analysis using SasView 5.0.6 software.

# 3 Results and discussion

Gel spinning is a specialized process used for obtaining polymers with high tensile strength and unique properties. This process is based on precipitation, where a suitable solvent is utilized to prepare a dope, and a non-solvent is employed in the coagulation bath to generate and maintain the fibrous structure. Since the polymer is extruded directly into the liquid, the filament experiences a greater drag force compared to extrusion in the air. This leads to extensional forces and, consequently, increased orientation of polymeric chains [28]. We adjusted the coagulation bath rotation rate to enhance orientation and reduce fiber diameters. Higher shear rates build up the orientation of the mTPU chains and create a robust scaffold. In contrast, at lower shear rates, silica particles create a chain-like structure between mTPU counterparts, increasing physical entanglements. These chain-like structures of silica can easily break and ultimately reconfigure to maintain a fibrous shape.

The physical properties of the solvent used in this work and the role of solvent type are detailed in Tables S2 and S3 of Supplementary Information. In comparison to typical solvents like THF and DMF, dioxane not only exhibits higher density and better performance in the coagulation bath but is also less miscible with the mTPU structure. Therefore,

dioxane was selected as the solvent, and specimens were prepared using this solvent with different concentrations of mTPU and SA. Consistent with our hypothesis, this solvent resulted in phase separation and the precipitation of solid components, leading to the formation of a fiber-in-fiber morphology with mTPU nanofibers embedded within the silica matrix. Digital images of the samples are provided in Fig. S3, and the trial formulations are discussed in Note S1 of Supplementary Information. In light of the initial experimental results as presented in movies S1, four samples highlighted in Table S1, demonstrated appropriate properties and, thereby, these samples were subjected to complete characterization. Because the ideal samples (T100-S100, T100-S75, T150-S100, T150-S75) were chosen based on fibrillation experience provided in Table S1, we conducted rheological, mechanical (DMA), and thermal conductance experiments for some other samples to scientifically approve our selection. Movie S2 depicts that decreasing the concentration of SA to less than 25 g·l$^{-1}$ causes disintegration in the coagulation bath, rendering the prepared mixture non-spinnable. For consistency in experiments, fibers with a diameter of 500 microns were chosen for investigation.

### 3.1 Rheological investigation and surface behavior

The physics of colloidal dispersions is influenced by a combination of hydrodynamic and thermodynamic interactions. Hydrodynamic interactions are contingent on factors such as temperature (affecting viscosity), particle shape, and shear rate. In contrast, thermodynamic interactions are tied to the surface area, composition, and equilibrium phase behavior. Aerogel fibrillation, much like other extrusion-based processing methods, necessitates a well-defined rheological solution with specific characteristics. Shear forces must reduce viscosity during processing, and after exiting the die, the materials must retain their shape until gelation occurs. Ideally, the solution should exhibit shear-thinning behavior during injection and maintain sufficient viscosity when subjected to minimal or no shear during gelation.

The crucial factor in achieving a continuous aerogel fiber structure is the rheological behavior of the solution as it exits the die. The spinning solution must rapidly transition into a solid state while preserving a fibrous morphology. This is markedly different from various polymer-based spinning processes, such as melt-spinning, which require a high-viscosity polymer melt to maintain the fiber structure. It also differs from the production of bulk aerogels, where the conversion process is definitely slow. The inclusion of a thickening agent in the recipe can reduce viscosity under shear stress and then restore it when the force is removed. Adjusting the shear-thinning behavior of the formula facilitates rapid solidification to achieve the desired fiber structure, preventing colloidal particles from dispersing [37–39].

Under low stresses, the structure remains intact, but when sufficient stress is applied, it is disrupted, displaying a liquid-like flow behavior. Then, briefly after removing stress, the shear-thinning structure can quickly return to its original solid-like state. It is equally important to control the gelation rate of silica aerogel fibers to avoid excessively rapid or gradual gelation, which can lead to issues such as clogging the needle or dissolution in the coagulating fluid. The introduction of a thickening agent promotes the sol-gel transition and helps regulate the gelation process [40].

Commonly used methods for rheological testing involve subjecting the sample to oscillatory or frequency-sweep shear flow, unveiling the viscoelastic behavior of a material. These experiments are also instrumental in investigating stability and identifying phase transitions. Strain-sweep tests, on the other hand, are typically employed to assess the shear-rate-dependent viscosity of a material, along with yielding and thixotropic behavior. In a few prior studies [38], researchers conducted strain-sweep or frequency-sweep rheological experiments to examine the impact of shear-thinning behavior on the final properties of aerogel materials. In terms of viscosity's role, it was observed that higher viscosity contributed to reduced aerogel shrinkage. However, to our knowledge, there has not been prior research focusing on the rheological influences on the in situ nanofibrillation of aerogels. Specifically, previous studies did not explore the impact of the elastic and viscous properties of gels on aerogel fibrillation. Consequently, the roles of complex viscosity of gels and the effects of shear-thinning behavior of polymeric solutions on aerogel fibrillation remain unexplored.

The results of frequency-sweep experiments for the various gels are depicted in Fig. 2. The rheological investigation highlights that samples exhibit shear-thinning behavior. As expected, an increase in SA content led to a significant rise in viscosity, as depicted in Fig. 2a. Comparing these results with those presented in Table S3, it becomes evident that SA plays a dominant role in shear-thinning, particularly at high SA concentrations. The results show that these hybrid samples display a non-Newtonian behavior and increasing SA content escalates the viscosity by three orders of magnitude higher than that of SA-free samples. Calculating the zero-shear viscosity for these specimens (Fig. 2b) illustrates a substantial increase with rising SA content, while mTPU's influence is relatively minor. Zero-shear viscosity curves show that 50 g·l$^{-1}$ of SA is the minimum value required to exhibit solid-like behavior.

Figure 2c clearly indicates that with an increase in SA content, the elastic portion of the response has intensified, and the gap between G′ and G″ has widened. This outcome can be attributed to the heightened gel entanglement resulting from the increased concentration of the components. This phenomenon bolsters the elastic characteristics of physical gels. For all these pastes, it is
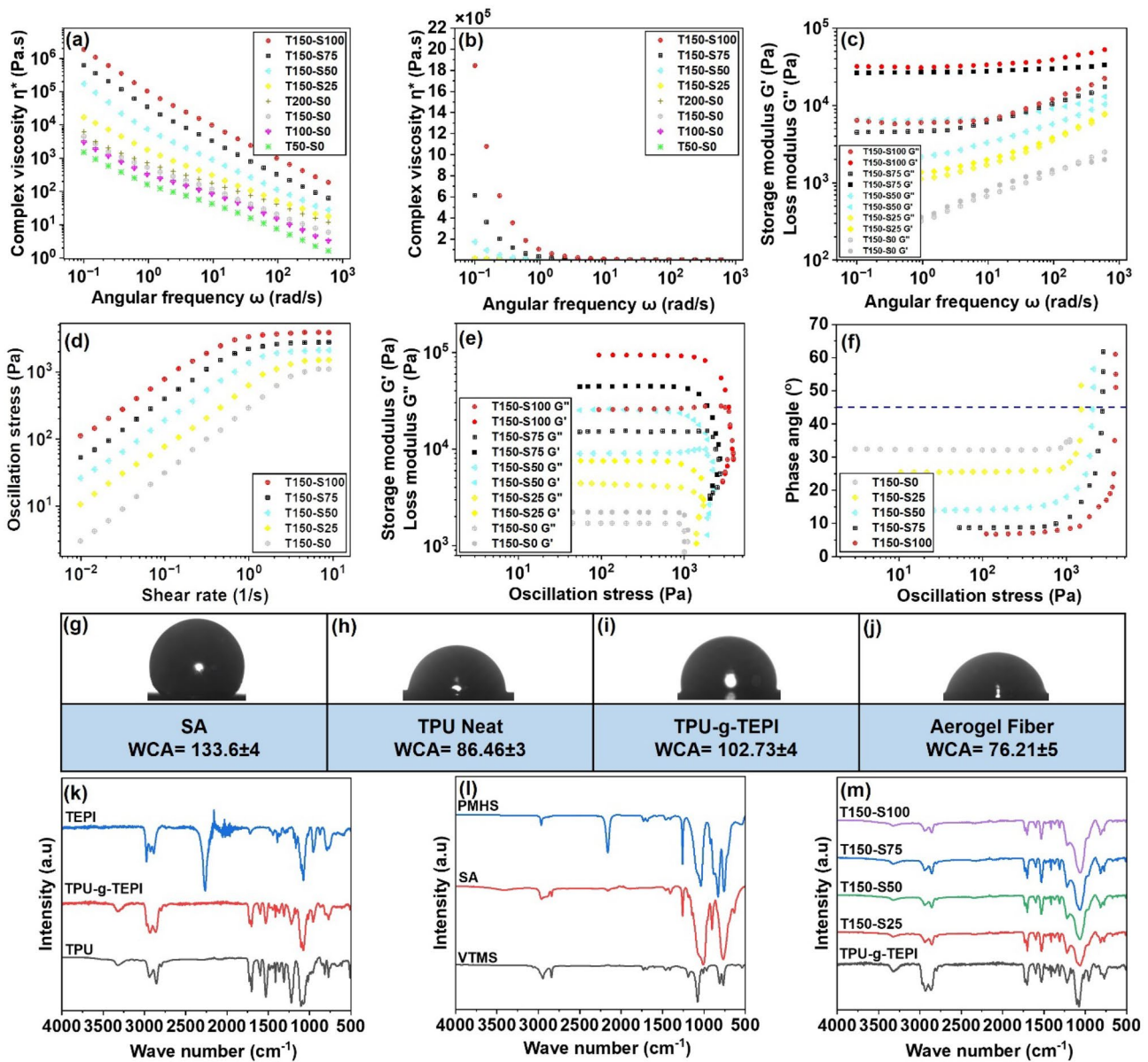
**Fig. 2** Rheological results in frequency-sweep experiments: **a** viscosity, **b** zero-shear-viscosity, and **c** viscoelastic behavior. Rheological results in strain-sweep experiments: **d** stress-shear rate, **e** viscoelastic behavior and yielding stress, and **f** phase angle and yielding stress. The water contact angle for **g** silica aerogel powder, **h** TPU neat, **i** TPU-g-TEPI, and **j** final aerogel fibers. FTIR spectra for approving **k** grafting process of TEPI on TPU chains, **l** grafting process of VTMS on PMHS, and **m** final chemical reaction between two components

noteworthy that they maintain their elastic gel network over a wide range of low frequencies, characterized by G′ consistently surpassing G″ (indicating solid-like behavior). For pastes with a high SA concentration, the modulus values become independent of frequency. This suggests that the formed physical gels provide a stable network and can be considered as permanent gels, where the gel's elastic nature (solid-like) consistently dominates over its viscous nature [38]. However, at higher frequencies, G′ and G″ eventually become equal, signifying the rupture of the

gel structure [41]. G′ increases with the concentration of SA, indicating a more elastic and stable gel network at higher SA concentrations, possibly due to the formation of more junction points with a greater quantity of components. This difference in concentration becomes less pronounced for samples with high SA content, likely due to slippage between SA particles. Even though all samples create the gel structure through junction zones formed by hydrogen bonding, samples with higher SA content exhibit significantly greater strength and can withstand oscillatory

stress at higher frequencies. Complex viscosity also tends to be higher in these samples, indicating a higher degree of interaction between polymer chains and SA particles [41].

Figure 2d–f illustrate the rheological behavior of pastes with varying compositions in strain-sweep experiments. Pure mTPU resin exhibits approximately shear-independent viscosity. However, as SA content increases, both viscosity and shear-thinning behavior become more pronounced. These results suggest that the initial high viscosity is due to the entanglement of mTPU and SA working against their own alignment (as shown in Fig. 2d). With higher shear rates and shear stresses, the structure aligns, leading to lower viscosity and a reduction in the force opposing movement (shear-thinning effect). This can be explained by the effect of aerogel particles on the solution's shear-thinning behavior. A higher concentration results in more connections between SA particles and mTPU chains, reducing ideal behavior and increasing shear-thinning behavior [38]. Figure 2d demonstrates that these fluids adhere to the Herschel-Bulkley law, which means they exhibit a non-zero-shear stress value even at a zero-shear rate, resembling the behavior of a solid more than that of a liquid.

The shear stress at zero-shear rate is called the yield stress. The yield shear stress is a critical parameter for these mixtures and arises from their non-Newtonian behavior. The yield stress increases with a larger concentration of aerogel or mTPU in the mixture. A higher yield stress implies that the material can withstand a greater force without flowing. The ability to bear a load is made possible because these fluids can alter their aggregation states, shifting from a free-flowing liquid to a quasi-solid state [42]. As we commence the injection of the mixture at a high shear rate, we surpass the yield stress, and the material transitions from a solid-like behavior to a flowing state [43, 44]. After leaving the nozzle, the aerogel fiber falls below the yield stress and retains its fibrous shape.

Figure 2e depicts the storage and loss modulus at different thickening agent concentrations, showcasing shear-thinning and yielding. Rheologically, an increase in SA content leads to significantly higher modulus values in the samples, indicating a greater degree of entanglement. These prepared pastes exhibit viscoelastic behavior, where the storage modulus surpasses the loss modulus. When the concentration is low, $G'$ is near $G''$, indicating liquid-like behavior. However, at higher concentrations, $G'$ substantially exceeds $G''$, reflecting solid-like behavior [37–39]. Polymer solutions experience stress associated with structure breakdown at the $G' = G''$ flow point. These plots reveal that all samples feature $G'$ higher than $G''$, signifying elastic dominance, and at higher stresses, the $G'$-$G''$ crossover, known as the yield stress, occurs [45, 46].

The phase angle, represented by delta ($\delta$), also serves as an indicator of whether the material exhibits characteristics more akin to a viscous substance ($\delta > 45$) or a solid-like material ($\delta < 45$) [47]. As the shear rate is progressively increased during the test until the material's structure yields, the phase angle detects structural changes. In the case of our pastes (as shown in Fig. 2f), we observe a plateau at lower stress levels, resulting in a phase angle value of approximately ten. However, as the stress levels increase, we witness an ongoing yield process where the material's structure begins to break down, causing the phase angle to approach ninety degrees. A lower phase angle suggests a better-developed material structure and the crossover of graphs with the 45-degree straight line marks the transition from a solid state to a liquid-like behavior. This transition point is also referred to as the $G'$-$G''$ crossover or the flow point. As illustrated in Fig. 2f, specimen T150-S100 exhibits a yield stress of around 6000 Pa, while T100-S75 exhibits a yield stress of only 1000 Pa. This means that T150-S100 is approximately six times stronger than T100-S75. It is evident that the sample T150-S100 yields significantly higher stress levels compared to the others.

In addition to rheological investigations, the interfacial behavior and thermodynamic interactions of the components were studied using a sessile test. It is essential to emphasize that the interface between the matrix and secondary phase plays a pivotal role in shaping the ultimate morphology of these hybrid materials. Shear resistance in these materials is provided by the interfacial tension between mTPU chains and aerogel particles. In fact, the increase in shear strength in these hybrid materials can be attributed to two primary phenomena: interfacial tension and the formation of physical bridges through silicon components, as well as the solvent absorption by the high-surface-area silica aerogel particles.

Water contact angle (WCA) not only plays an indispensable role in studying the interfacial behavior and thermodynamic interactions of the components, but it also helps predict the warmth retention and the deterioration of thermal insulation performance caused by moisture [48]. Grafting TEPI onto the surface TPU chains introduces hydrophobic ethoxy groups, leading to an increase in WCA. However, hydrolysis reactions in water and crosslinking eliminate these hydrophobic groups from the surface, causing the WCA to decline to approximately 76 for aerogel fibers. The water contact angle (WCA) for the various components used in this study was assessed and is presented in Fig. 2g–j. The wettability and washability of the specimens were analyzed in cold (25 °C) and warm (60 °C) water [49]. To prove the washability of these fibers, samples were immersed in water for several times, and the WCA was calculated by removing the samples from water and drying them in an oven at 80 °C for 30 min before WCA measurement [50]. Consistent with FTIR results, these experiments confirm that all functional groups reacted, and the surface characteristics reached a stable condition without noticeable changes in WCA, as presented in Fig. S4.

The results of the water contact angle (WCA) tests reveal that SA exhibits hydrophobic characteristics, while TPU and mTPU are relatively hydrophilic. Consequently, in this three-phase system, there are two solid phases and a liquid one (dioxane), with limited miscibility. In the absence of external forces, the liquid phase is strongly retained within the SA particles. This results in the creation of a well-defined structure comprised of mTPU and aerogel particles, effectively behaving like a solid. However, when an external force is applied, the third phase is displaced from within the particles, facilitating the lubrication of adjacent particles' movement amidst the mTPU chains. This transformation turns the mixture into a liquid, aligning the mTPU chains between the SA particles.

## 3.2 Chemical crosslinking evidence and morphological structure

The successful grafting reactions are clearly evident in the FTIR and $^{1}$H NMR graphs. As shown in Fig. 2k, Fig. S5 and discussed in Note S2, grafting TEPI onto the TPU chains leads to the involvement of N-H groups, which then react with the isocyanate functionality of the silane, resulting in a shift in their peak. In the FTIR spectra, we can observe the presence of a vibrational bond at 1080 cm$^{-1}$ attributed to the stretching of Si-O-C bonds [51], as well as a broad absorption peak in the range of 3200–3400 cm$^{-1}$, assigned to the N-H stretching of the urethane linkage, and other urethane-related features [52–54]. The absence of the silane isocyanate (N=C=O) stretching band at around 2275 cm$^{-1}$ and the ethoxy silane pendant groups indicates that the isocyanate groups underwent reactions during the compounding procedure, confirming the success of the grafting reaction [55–59]. These changes are indicative of chemical transformations taking place.

Furthermore, the results obtained and presented in Fig. 2l and S6 provide compelling evidence of the successful grafting reaction between VTMS and PMHS. An initially narrow peak observed at 2160 cm$^{-1}$, corresponding to the Si-H group [60], vanishes completely when grafting reaches 100%. Additionally, upon closer inspection of the region around 1600 cm$^{-1}$, it is evident that the vinyl group has been entirely consumed in the aerogel samples, suggesting the absence of carbon-carbon double bonds in these materials [61]. A faint peak at 2840 cm$^{-1}$, associated with ethoxy groups, is also observable [62]. A sharp peak at 1000 cm$^{-1}$ is attributed to the Si-O-Si bond. As the reactions progress, the intensity of peaks related to unreacted OH groups and C=C bonds decreases, while the height of the Si-O-Si peaks increases, signifying the advancement of the reaction [63]. This detailed analysis reveals the presence of residual ethoxy groups in the aerogel particles. This observation is significant as it suggests that these particular aerogels retain

functional groups, rendering them receptive to participation in hydrolysis and condensation reactions with TPU-g-TEPI.

The FTIR results, as illustrated in Fig. 2m, strongly support the occurrence of the final reaction between mTPU chains and SA particles, as evidenced by the disappearance of ethoxy groups in aerogel fibers.

The morphology and structural properties of the samples were revealed using SEM, XRD, and N$_2$ absorption-desorption techniques. Figure 3 shows the SEM morphology of the in situ fibrillated mTPU-SA aerogel fibers. Fiber cross-section, fiber-in-fiber morphology, and phase separation are presented in these figures. Low magnification images reveal that the surface of the filament is rather uniform and smooth, confirming that the processing condition is appropriate. High-magnification images from the surface of developed aerogel fibers support our hypothesis and demonstrate that mTPU nanofibers are predominantly aligned in the tensile direction. As evident, phase separation has generated a macroporous morphology between the mTPU nanofibers, while the SA with a mesoporous structure (Fig. S7) encapsulates these developed nanofibers. The standard deviation of the fiber diameter was as low as 10% of the average and the images show that adjusting rheological properties can guarantee the fiber roundness and final cross-section shape. In this process fiber cross-section depends on the ratio of the evaporation rate of the first solvent (dioxane) and the diffusion rate of the second solvent (water). As shown in Fig. 3m–o and movies S1, when this ratio is approximately 1, the final cross-section is circular, when it is less than 1, disintegration occurs. For values more than 1, shrinkage occurs, and serrated or peanut-shaped fibers will be produced. By increasing the SA concentration, shrinkage is controlled better leading to circular cross-section; on the other hand, the number of nanofibrous mTPU in the structure has decreased gradually.

To further investigate the developed structure with these organic-inorganic counterparts, EDAX (energy-dispersive X-ray analysis) images of elemental mapping were obtained and presented in Fig. 4a–g. The qualitative characterization [64] and mapping micrographs indicate the presence and distribution of four dominant elements including carbon, silicon, oxygen, and nitrogen.

The pore size distributions, surface area, and isotherms of the specimens are presented in Fig. 4h–k. We employed density functional theory (DFT) to compare the pore size distribution for these samples. The obtained isotherms exhibit the typical IV-type curves, characterized by a narrow hysteresis loop according to IUPAC standards, which further confirms the mesoporous nature and mechanical robustness of the structure, displaying low deformation during N$_2$ adsorption-desorption cycles [20, 65]. In all samples, we observed two predominant peaks in the pore size distribution with approximate diameters of 6 and 30 nm, mirroring the
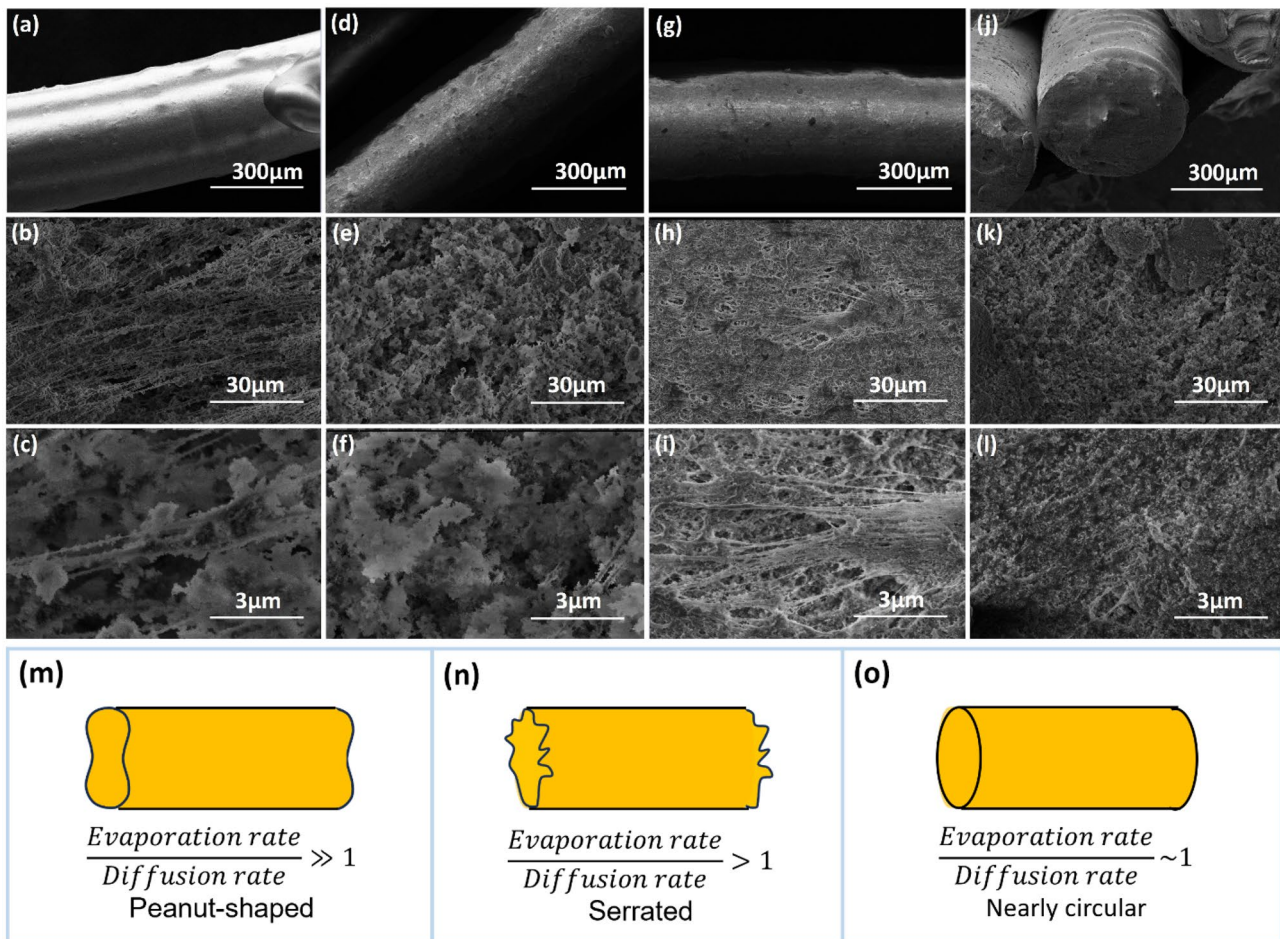
**Fig. 3** SEM images of samples at different magnifications: **a–c** T150-S75, **d–f** T150-S100, **g–i** T100-S75, **j–l** T100-S100. Polymer-colloid mixture: **m–o** the possible effect of evaporation-diffusion rates ratio on the cross-section of fibers

original APH100 [31]. These findings affirm that there was minimal shrinkage during the reprocessing of these aerogel materials. Different interface properties acted as barriers, limiting the molecular movement of mTPU chains into the porous aerogel structure and consequently preventing a decrease in pore diameter. This average pore size also suggests that the aerogel skeleton exhibits remarkable compression strength, allowing it to withstand the capillary pressure during the drying stage without densification, effectively springing back to its original state.

However, it is worth noting that we observed a significant variation in the formation of macropores during the drying process. As the mTPU content increased, the amount of $N_2$ absorption decreased, resulting in a decline in pore volume and surface area, in line with our expectations. This particular phenomenon significantly influenced the surface area, as depicted in Fig. 4i, even though the pore volume and pore size distribution remained relatively consistent (Fig. 4j–k). This discrepancy can be attributed to the variations in

shrinkage and the interaction of mTPU chains among the different samples. In fact, the increased affinity of mTPU chains at higher concentrations hindered the formation of additional mesoporous pores, leading to an increase in surface area with increasing SA content.

$N_2$ absorption-desorption technique primarily targets micro and mesopores (those with widths smaller than 100 nm) in materials featuring a nanoporous structure and may not fully capture larger pores [66, 67]. However, the aerogels obtained in this work demonstrate a complex structural morphology of micro, meso, and macropores [68], as confirmed by the SEM images and DFT results. On the other hand, flexible porous materials, such as foams and aerogels, may not offer reliable stability against mercury intrusion. Consequently, the application of pressure during mercury intrusion may cause deformation or collapse of the flexible porous structure, further complicating the analysis [69, 70]. Therefore, to provide a more accurate measurement of the average pore diameter while minimizing the influence of the flexible structure's mechanical
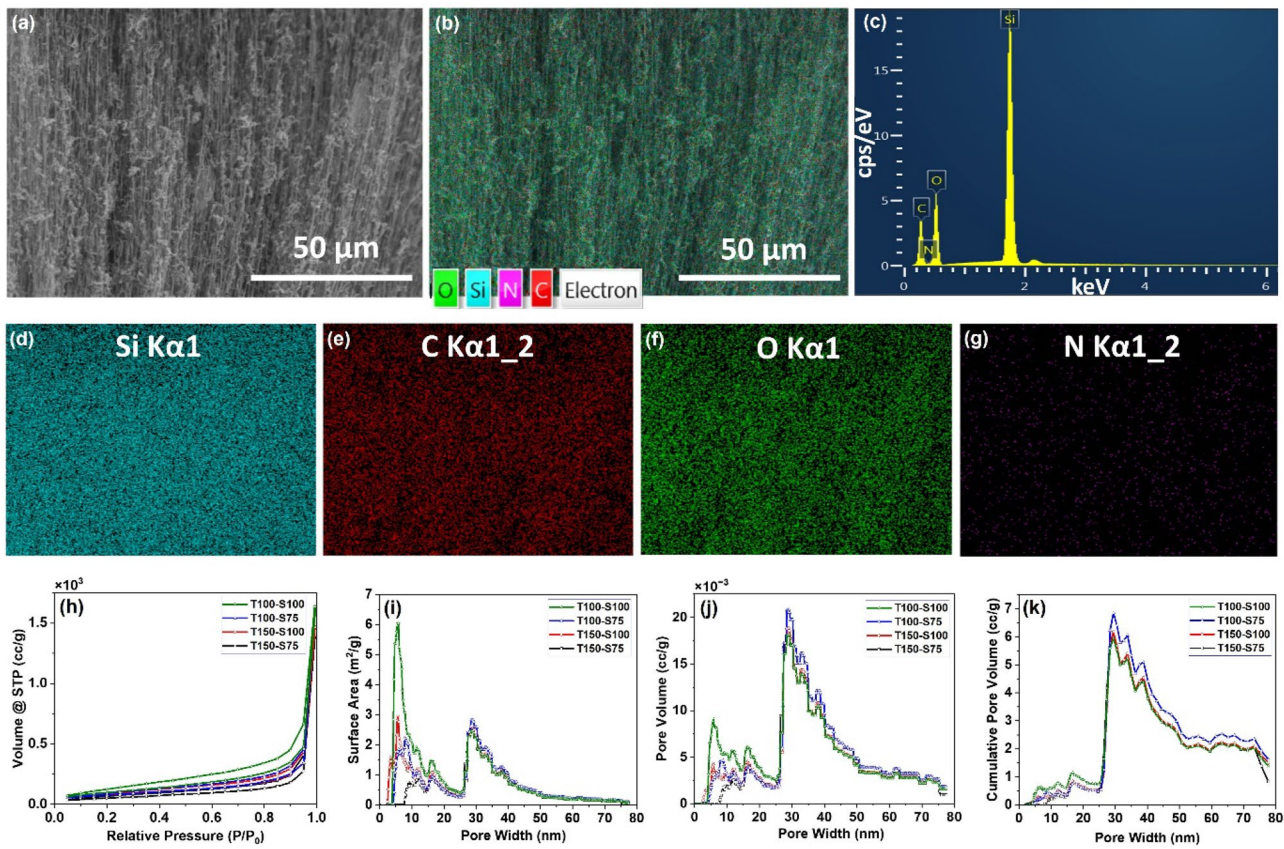
**Fig. 4** **a**, **b** EDAX images of specimen T150-S75 and **c** atomic percent of different elements. Elemental mapping of T150-S75: **d** silicon, **e** carbon, **f** oxygen, and **g** nitrogen. $N_2$ absorption-desorption results: **h** isotherm hysteresis, **i** surface area, **j** pore volume, and **k** cumulative pore volume

deformation during these experiments, we calculated the average pore diameter using Eqs. 1–3 [71]. The results presented in Table 1 confirm a clear relationship between porosity, surface area, and the SA/mTPU ratio, while pore size is a function of SA content.

$$\epsilon(\%) = \frac{^1/\rho_b - ^1/\rho_s}{^1/\rho_b} \times 100 \tag{1}$$

$$V_p\left(\frac{cm^3}{g}\right) = {^1/\rho_b} - {^1/\rho_s} \tag{2}$$

$$D_p(nm) = 4V_p/S \tag{3}$$

where $\epsilon$, $V_p$, $D_p$, $\rho_b$, $\rho_s$, and $S$ are porosity, pore volume, pore diameter, bulk density, skeleton density, and surface area, respectively. Skeleton density was calculated based on mTPU and SA concentration and their densities which are 1.11 and 1.006 g·ml$^{-1}$, respectively.

**Table 1** Calculated characteristics of the specimens based on $N_2$ absorption results

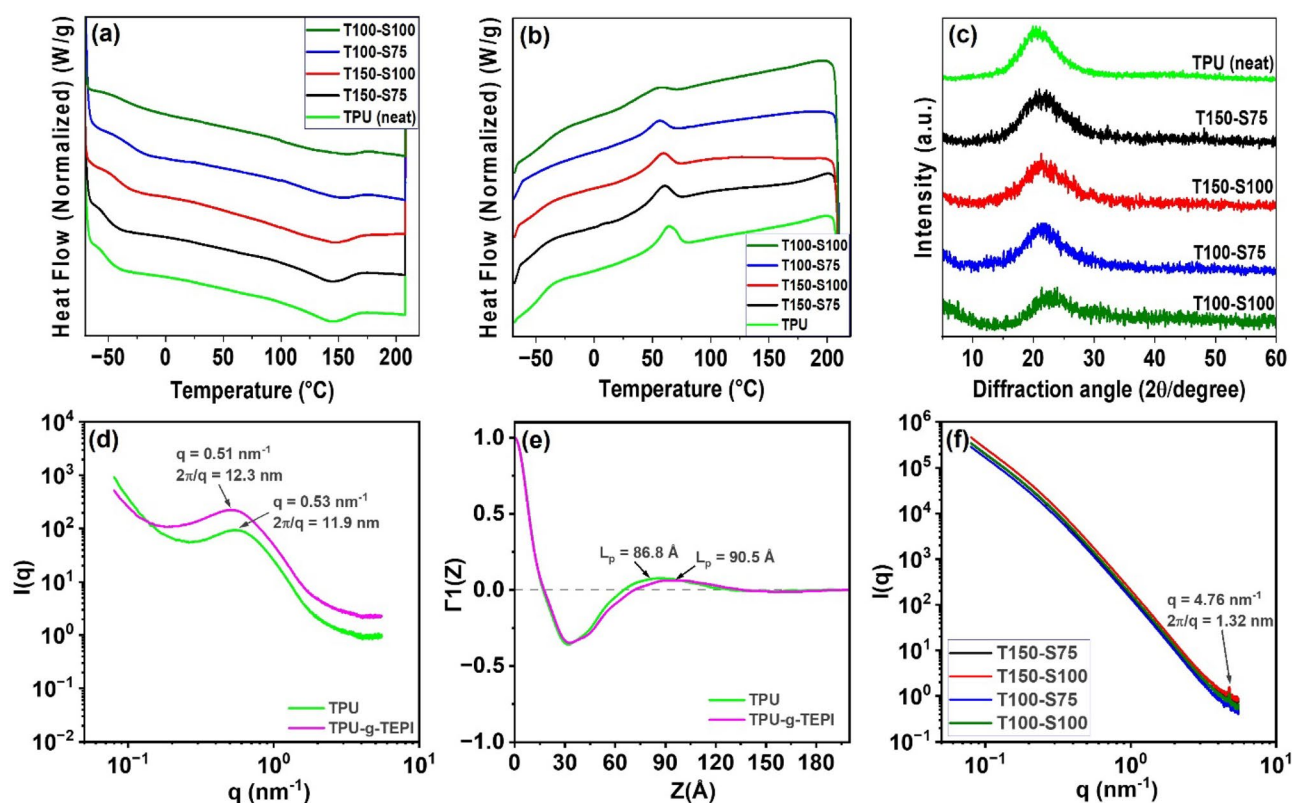| Sample code | mTPU/SA Ratio | $\rho_b$ g·ml$^{-1}$ | $\rho_s$ g·ml$^{-1}$ | $\epsilon$ % | $V_p$ cm$^3$·g$^{-1}$ | $S$ M$^2$·g$^{-1}$ | $D_p$ nm |
|---|---|---|---|---|---|---|---|
| **T100-S100** | 50/50 | 0.211 | 1.058 | 80.057 | 3.79 | 350.15 | 43.34 |
| **T100-S75** | 57/43 | 0.195 | 1.065 | 81.695 | 4.19 | 273.44 | 61.29 |
| **T150-S100** | 60/40 | 0.263 | 1.068 | 75.384 | 2.87 | 269.65 | 42.52 |
| **T150-S75** | 67/33 | 0.251 | 1.076 | 76.666 | 3.05 | 210.4 | 58.07 |

**Fig. 5** DSC curves for hybrid samples in **a** first heating ramp and **b** cooling ramp, **c** XRD graphs, **d** 1D SAXS plots of TPU and TPU-g-TEPI generated from 2D SAXS pattern, **e** long-period calculation using 1D SAXS data, and **f** 1D SAXS plots of various hybrid aerogel fiber samples

## 3.3 Thermal analysis

Consistent with SEM images, DSC graphs presented in Fig. 5 confirm phase separation, stress-induced orientation, and crystallization of mTPU chains in the final structure. TPU is a semi-crystalline material, hence, tends to unfold, orient, and crystallize in the flow direction. At high shear rates, viscosity drops and the TPU chains have enough mobility, and they can deform easily [72, 73]. On the contrary, chemical crosslinking reactions and homogenous distribution of the TPU chain at a molecular level can significantly decrease the crystallization and consequently affect the thermal behavior of the TPU chains [9]. It is well known that an increase in spinning speed increases the orientation of molecular chains along the fiber axis, resulting in significantly different thermal behavior. After drawing, fibers may relax and recover some part of the deformation. On the other hand, when they leave the die and there is no stress, viscosity rises sharply and due to limited mobility, polymer does not have enough time to relax from the drawing stresses and show flow orientation behavior. Chain orientation in flow direction increases crystallinity in crystalline polymers. It is also possible that the in situ nanofibrillation of mTPU alters the crystallization kinetics, and crystal size and shape.

In general, stress-induced nanofibrillation slightly enhanced crystallization compared to commonly produced TPU fibers.

DSC results for heating and cooling ramps are presented in Fig. 5a and b, and thermal properties and crystallinity percentages of the specimens are summarized in Table 2. As reflected in the heating cycle, the glass transition temperature ($T_g$) increased slightly from −41.31 to −36.83 °C, revealing the crosslinking procedure between these components enhanced the immobilization of the amorphous section of the developed structure. In the same way, the melting temperature ($T_m$) shifted from 151.47 to 159.69 °C as expected. An increase in the melting point is due to stress-induced orientation during fibrillation causing an increase in chain packing and reduction in free volume. Therefore, the perfect crystalline structure inside mTPU nanofibers developed during phase separation led to a higher melting point. Nevertheless, in the second ramp, crystallization in mTPU occurs without exterior force where crosslinking hinders the recrystallization process and crystallization temperature shifts to lower temperatures [74]. These reductions in $T_C$ and increases in $T_m$ can be attributed to the effect of processing conditions on the crystallization process and mobility of the mTPU chain segments because of the orientation and the crosslinking process. The calculated $\Delta H_m$ declined gradually

**Table 2** $T_g$, $T_m$, and the related enthalpies of the pure TPU and hybrid specimens

| Sample code | mTPU/SA | $T_C$ | $\Delta H_C$ | Normalized $\Delta H_c$ | $T_m$ | $\Delta H_m$ | Normalized $\Delta H_m$ | $T_g$ |
|---|---|---|---|---|---|---|---|---|
| | Ratio | °C | J·g$^{-1}$ | J·g$^{-1}$ | °C | J·g$^{-1}$ | J·g$^{-1}$ | °C |
| **TPU neat** | 100/0 | 68.62 | 7.58 | 7.58 | 151.47 | 8.99 | 8.99 | −41.31 |
| **T150-S75** | 67/33 | 63.36 | 5.42 | 8.13 | 152.8 | 7.49 | 11.26 | −40.06 |
| **T150-S100** | 60/40 | 61.29 | 5.2 | 8.68 | 154.11 | 7.05 | 11.77 | −37.69 |
| **T100-S75** | 57/43 | 59.06 | 4.18 | 7.32 | 156.56 | 5.78 | 10.12 | −37.44 |
| **T100-S100** | 50/50 | 58.39 | 3.86 | 7.72 | 159.69 | 4.81 | 9.62 | −36.83 |

from 8.99 to 4.81 J·g$^{-1}$. However, the normalized values for this characteristic ($\Delta H_m$ divided by mTPU concentration) remarkably increased for aerogel fibers exhibiting induced crystallization of these fibers due to fibrillation and precipitation (phase separation) stresses. This is consistent with the SEM images, where nanofibrous mTPU was found in hybrid samples. The XRD curves shown in Fig. 5c also indicate that the crystalline structure of TPU has not changed notably after the addition of SA. This confirms that orientation, and consequently crystallization, which significantly affects mechanical properties, has occurred in mTPU nanofibers.

SAXS and WAXS were also employed to trace the structural changes occurring in hybrid fibers and to gain insight into the material's structure [75]. Figure 5d displays the 1D SAXS plots generated by integrating the 2D SAXS patterns over azimuthal angles ranging from 0° to 360°. A broad peak around the scattering vector ($q$) value of 0.53 nm$^{-1}$ with a d-spacing of 11.9 nm was observed for neat TPU, attributed to the presence of oriented crystals. After grafting, the peak shifted to a slightly lower q (0.51 nm$^{-1}$), while the d-spacing increased to 12.3 nm. The increase in d-spacing indicates that the distance between two oriented crystals increased due to the presence of grafted TEPI. To further verify this, we calculated the long periods of the crystals for the materials. As depicted in Fig. 5e, the long-period value increased from 8.68 to 9.05 nm after grafting. Nevertheless, grafting did not noticeably impact the degree of orientation of the TPU crystals [76].

The 1D SAXS plots for hybrid aerogel fibers are presented in Fig. 5f. As observed, the broad peak related to TPU-oriented crystals disappeared, and a new peak emerged in the high q region with a d-spacing of 1.32 nm. This new peak could be associated with packed TPU crystals inside the nanofibrous TPU phase within the hybrid aerogel fibers. The appearance of new relatively ordered scattering peaks at low angles indicates the formation of a new crystalline phase during fibrillation [77]. Note that a peak related to the oriented TPU nanofibers was not detected in Fig. 5f. This is because the distance between aligned fibers is approximately 300 nm (as evidenced by SEM). The thermodynamic incompatibility of the two components and approximately 85% porosity in these aerogel fibers give rise to the distance

between two hard domains, leading to an increase in the long period [78]. Due to instrumental limitations, the lowest $q$ value obtained was 0.08 nm$^{-1}$, translating to a d-spacing of 78.54 nm. Therefore, a peak related to oriented nanofibers was not detected herein. Consistent with DSC and XRD results, there is no obvious change in 1D WAXS results of the samples presented in Fig. S8.

To further explore the temperature range of application, we subjected the samples to dynamic mechanical analysis (DMA). The mechanical performance of the hybrids under dynamic loading conditions was evaluated over a temperature range spanning from −60 to 180 °C, as shown in Fig. 6a. From the storage modulus (E′) curves depicted in Fig. 6a, we observe the typical three-stage behaviors. The glassy state of pure TPU exhibits the highest value. Conversely, with an increase in the SA content, the storage modulus (E′) values sharply decrease, eventually plateauing for the T50-S100 sample. Compared to TPU with a $T_g$ of −41 °C, PMHS has a $T_g$ around −150 °C, thereby increasing SA content, extending the rubbery state to lower temperatures and consequently, the temperature range of application increased significantly. The $T_g$ was determined from the tan ($\delta$), as shown in Fig. 6b. In accordance with DSC curves, $T_g$ has occurred somewhere between −50 and −20 °C and slightly shifted to a higher temperature, likely due to the crosslinking process. In the rubbery state, by increasing SA content, modulus decreased as well. Therefore, the wearing comfort of these fibers has increased. Because wearing comfort has an inverse relationship with the modulus of elasticity, based on the following equations [49]:

$$\text{Wearing comfort} \sim \text{Euler's buckling load} \sim \frac{1}{EI} \quad (4)$$

$$I = \frac{\pi D^4}{64} \quad (5)$$

where $E$, $I$, and $D$ are the modulus of elasticity, the moment of inertia, and the diameter of the fibers, respectively.

Additionally, the crosslinked TPU chains exhibit resistance to melting and sticky behavior at higher temperatures, allowing most samples to maintain their mechanical
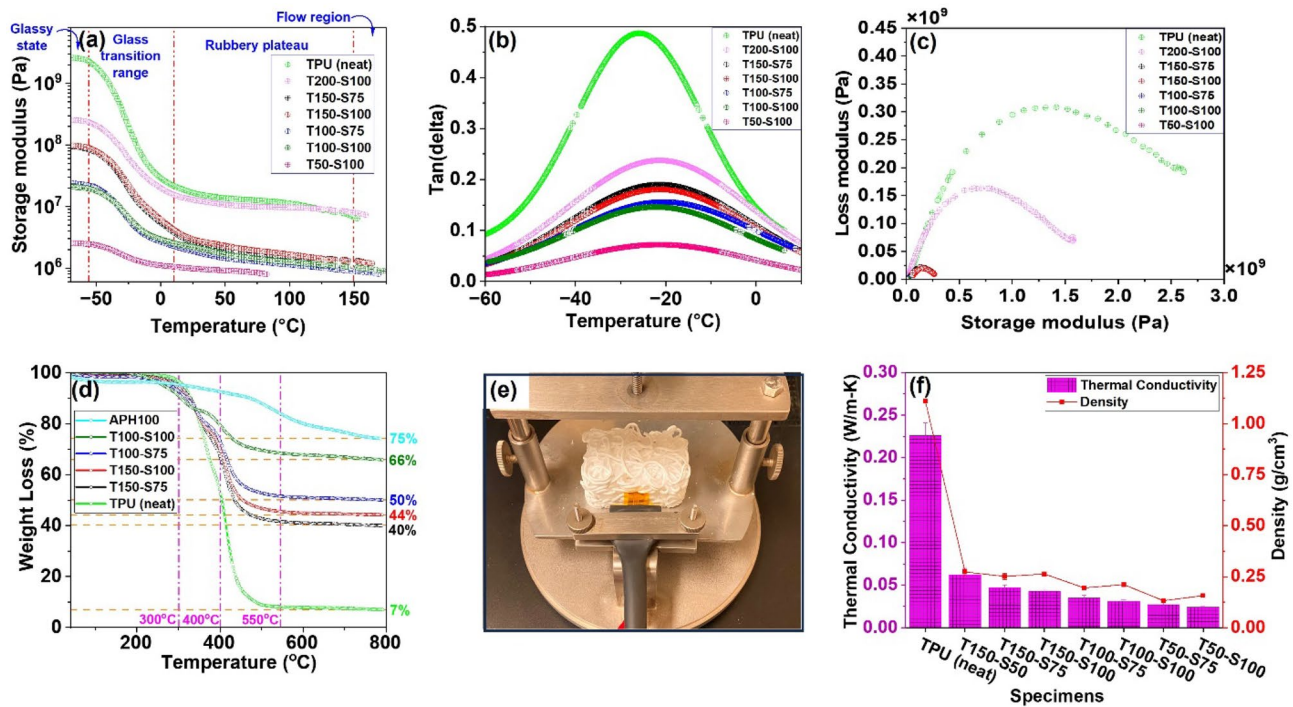
**Fig. 6** DMA analysis of the specimens: **a** storage modulus, **b** tan (δ), and **c** Cole – Cole curves. **d** TGA analysis for the samples under N₂ covering a temperature sweep from room temperature up to 800 °C, **e** specimen for thermal conductivity experiments, and **f** thermal conductivity of the specimens together with their density

strength (E′) even up to 150 °C. Therefore, the developed TPU-SA structure achieves an extended temperature range of performance.

DMA experiments also provide insights into the viscoelastic response of a material, serving as an indicator of system homogeneity through the Cole-Cole curve. A perfect semicircular curve denotes the preparation of a homogeneous system, whereas an irregular or imperfect semicircle points to a heterogeneous system. Figure 6c displays the Cole-Cole curves, showing the relationship between the loss modulus and storage modulus for these aerogel fibers. Notably, all samples displayed imperfect semicircles, confirming a heterogeneous system with well-distributed components, which aligns with the findings from SEM images [79].

In order to elucidate the thermal stability of the developed aerogel fibers, we conducted a TGA test. Figure 6d displays the TGA curves of the mTPU-SA hybrid series under a nitrogen atmosphere, covering a temperature range from room temperature to 800 °C. Notably, all samples exhibited almost no weight loss below 200 °C, indicating effective inhibition of water absorption in these hybrid materials. Weight loss processes became significant above 300 °C and occurred in two stages. In the first stage, roughly half of the degradation, including small molecules and functional groups, occurred up to 400 °C. As the temperature increased, the remaining parts of the structure began to decompose, resulting in sharp

drops in the curves after 400 °C [65]. These data clearly demonstrate that the presence of SA particles provided protection to the mTPU nanofibers, leading to delayed degradation and a shift towards higher temperatures, especially with an increased SA content.

The other striking feature of aerogel fibers is their low thermal conductivity. The density and thermal conductivity of the samples are displayed in Fig. 6f. Theoretically, the thermal conductivity of a porous fiber is determined by the sum of thermal convection, solid and air conduction, and thermal radiation. Heat convection and gas conduction are restricted by the nanostructure of the aerogel. For the radiation part, heat is radiated mainly by invisible infrared light and because a porous fiber can largely improve the reflectance of infrared light, the thermal radiation becomes negligible. The propagation of phonons, which are responsible for thermal conductivity, in an aerogel skeleton dramatically decreases because of the tortuosity of the pathway [80, 81].

To measure the thermal conductivity of prepared aerogel fibers, samples were stacked and knitted together using a hot needle to have a mat-shaped structure with a minimum of 5-mm height, as shown in Fig. 6e. The sensor of the machine was placed directly between two layers of specimens [82]. The thermal conductivity was calculated from the average result of the anisotropic stacked method of the machine. The results present a normal decreasing

trend with the increase of SA content and reach the optimal value of 0.024 W·m$^{-1}$·k$^{-1}$. Greater thermal conductivity is achieved with higher mTPU content due to increased orientation, resulting in a denser hybrid aerogel structure. This densification reduces porosity, thereby enhancing the thermal transfer capacity of the material [83]. This can be explained by the fact that the heat transfer through the continuous mTPU chains might be dominant for these samples, in comparison with the heat transfer through the discontinuous aerogel phase, leading to higher thermal conductivities [20]. At the same time, the larger pore size in these samples also increases the gaseous thermal conduction. This is in line with the results described in other works [65]. As the aerogel volume fraction increased, the thermal conductivity significantly decreased due to the declining trends in density, orientation, and crystallinity [20]. Concurrently, more SA led to higher porosity and thereby higher tortuosity in the solid structure. In overall, increasing SA content restricts all three mechanisms of thermal conduction causing a decline in the thermal conductivity of the specimens.

## 3.4 Mechanical properties

The formation of molecular orientation and crystalline structure plays an important role in the ultimate mechanical properties of the fibers. Molecular orientation arises from the parallelization of the molecular chains along the fiber axis in both the crystalline and non-crystalline regions. To probe the mechanical performance of developed aerogel fibers, we evaluated these samples in tension mode using an Instron machine. Specimens were fixed between two layers of sticker paper, as shown in Fig. 7a, to address challenges like slippage in the grips and grip effects [84]. Ultimate tensile strength (UTS) and elongation at break (EAB), presented in Fig. 7b and c, approve that orientation of molecules in fiber direction and nanofibrous mTPU generation has a vital effect on the mechanical properties. The alignment of molecular chains along the fiber axis enhances the UTS, EAB, and modulus of the fibers.

Samples with higher concentrations of mTPU had better mechanical properties. The UTS and EAB were 10.26 MPa and 100.94% for samples with 67% mTPU, while these values dropped to 3.7 MPa and 40.56% for samples with 50% mTPU. Indeed, reducing the mTPU concentration by 25.37% led to a significant decrease in both the UTS and EAB for these samples. Specifically, the UTS decreased by 63.94%, and the EAB dropped by 59.82%. This can be due to a reduction in nanofibrous concentration in the axial direction of fibers and a decline in the average molecular weight of the final hybrids. Although SA particles act as a crosslinker between mTPU nanofibers, the developed structure gets its strength from both network formation and entanglements. Thus, the applied stress on the fibers needs to be transferred

and tolerated with the nanofibrous network of mTPU rather than SA. Consequently, mechanical properties such as UTS and EAB can be enhanced significantly by increasing mTPU concentration [41]. The fluctuation in the results may be caused by the inhomogeneous structure of the mTPU skeleton and porous SA during the tensile test [20, 65]. It is also possible that phase separation between mTPU chains and SA particles is more dominant in samples with higher concentrations of mTPU, inducing more voids between the chains, which allows better movement and rearrangement of the chains and thus higher mechanical properties [41, 85].

In order to assess the effects of adding different concentrations of SA to mTPU on fatigue and ratcheting responses of the mTPU-SA aerogel fibers, varying load levels were applied to the samples in the range of 50–80% of the samples' ultimate tensile strength values. Figure 7d shows the S-N curves of the samples, indicating that samples containing a higher amount of mTPU experienced higher fatigue lives. This was expected, because increasing the amount of mTPU results in higher stiffness and ductility, leading to higher fatigue strength. Conversely, SA particles impart a local and progressive fatigue damage mechanism causing a decline in the fatigue life. The reason behind this is that SA is made of a low molecular weight polymer with a fractal structure that contributes more to compression mode rather than tension [31]. Furthermore, unoriented SA particles deform inelastically even under low loads and demonstrate plastic deformation.

To predict the fatigue life of any structure like a textile made up of this aerogel, which will most likely be under different tensile cyclic loading, identifying strain-based fatigue parameters of these aerogel batches is essential. To do so, first, the S-N data presented in Fig. 7d which have been obtained under zero-to-tension stress condition ($R = 0$) were converted to the completely reversed stress condition ($R = -1$) using Smith-Watson-Topper (SWT) parameter [86]:

$$\sigma_{ar} = (\sigma_a \sigma_{max})^{1/2} \tag{6}$$

where $\sigma_{max}$ is the maximum applied stress, $\sigma_a$ is $\frac{\sigma_{max}}{2}$ when $R = 0$, and $\sigma_{ar}$ is the equivalent stress amplitude at a fully reversed stress condition. The fatigue life would be the same when $\sigma_{ar}$ equals the SWT parameter at any given stress ratio. Then, elastic and plastic strain components were extracted from the true stress-strain curves of each sample and plotted versus the number of cycles to failure. The elastic and plastic data in log-log $\epsilon - N$ plots should lay on straight lines according to the Manson-Coffin strain-based fatigue model [87]:

$$\epsilon_a = \epsilon_a^e + \epsilon_a^p = \frac{\sigma_f'}{E}(2N_f)^b + \epsilon_f'(2N_f)^c \tag{7}$$
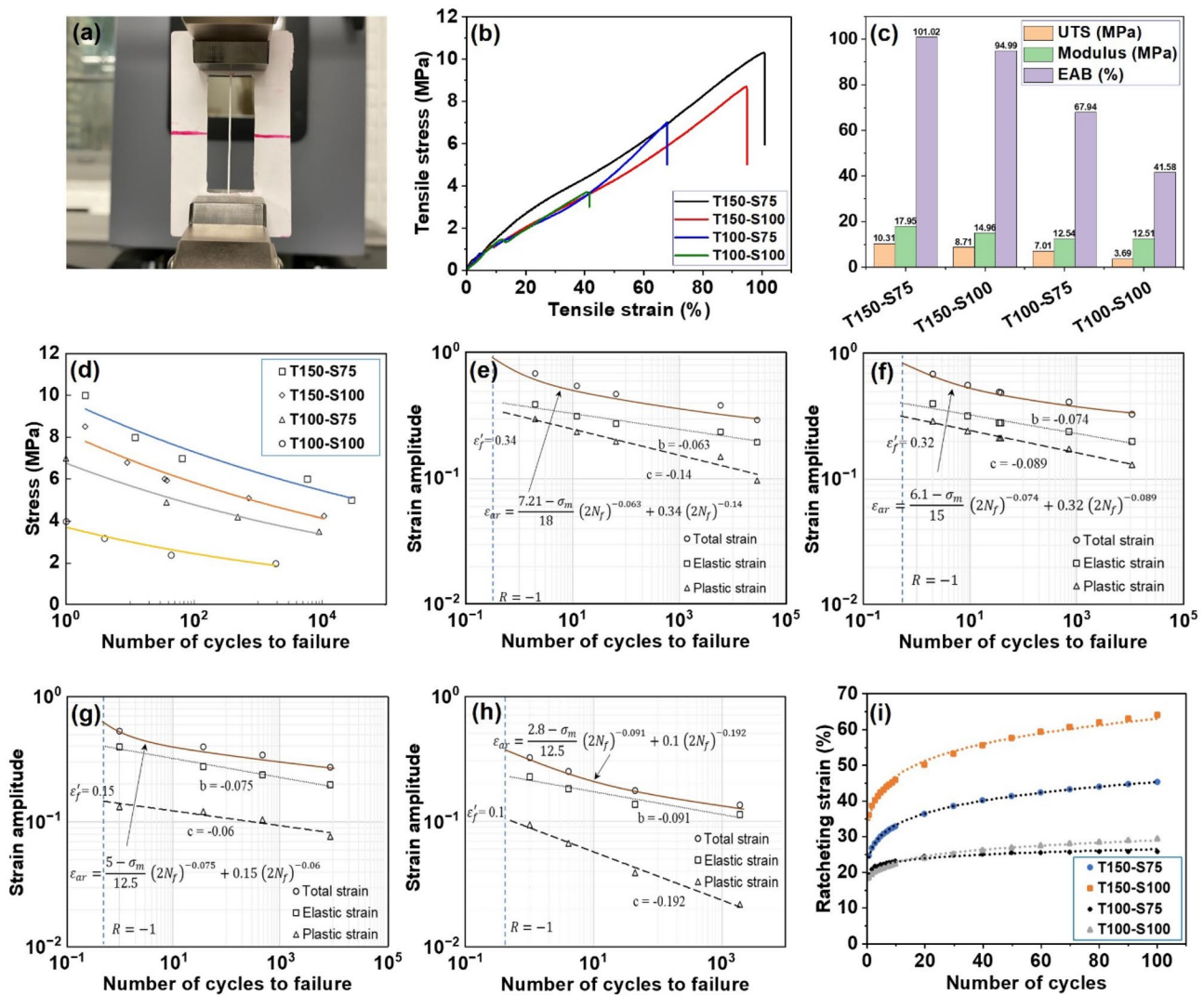
**Fig. 7** **a** Sample preparation for mechanical testing. **b** Tensile stress-strain curves for all series of specimens. **c** Static values for specimens in tension mode. **d** S-N curves of different combinations of mTPU-SA aerogel fibers. **e–h** Strain-based fatigue parameters of the mTPU-SA aerogel fiber samples: **e** T150-S75, **f** T150-S100, **g** T100-S75, and **h** T100-S100. **i** Ratcheting response of the mTPU-SA samples at 50% of UTS

where $\epsilon_a^e$ and $\epsilon_a^p$ are elastic and plastic strain amplitudes, $\sigma_f'$ and $b$ are fatigue strength coefficient and exponent, and $\epsilon_f'$ and $c$ are fatigue ductility coefficient and exponent, respectively. Figure 7e–h illustrate how the above-mentioned strain-based fatigue parameters have been extracted, and the extracted data are summarized in Table 3. As seen in these figures, for all batches of the samples, the portion of elastic strains contributes more than plastic strains, and this has been observed for all load levels. Indeed, the transition fatigue life, characterized by the intersection of elastic and plastic strain lines, has not been observed for any of them. This is in contrast with most thermoplastic materials in which the transition fatigue life varies in the range of 20 to 400 cycles [88].

Ratcheting is the accumulation of strain values when the part is subjected to a cyclic load with non-zero mean stress and is defined as follows:

$$\epsilon_r = \frac{(\epsilon_{max} + \epsilon_{min})}{2} \tag{8}$$

where $\epsilon_r$ is the ratcheting strain accumulation, and $\epsilon_{max}$ and $\epsilon_{min}$ are the maximum and minimum strain values at each cycle. Figure 7i depicts the ratcheting response of the mTPU-SA samples subjected to 50% of their UTS value. As seen, samples containing lower concentrations of SA possessed the lower ratcheting strain accumulation, and this is more noticeable in the samples with higher contents of mTPU.

**Table 3** Static and strain-based fatigue test data for all batches of mTPU-SA aerogel fiber

| Samples code | Modulus of elasticity (MPa) | Load ratio (R) | Fatigue strength coefficient $\sigma'_f$ (MPa) | Fatigue strength exponent $b$ | Fatigue ductility coefficient $\epsilon'_f$ | Fatigue ductility exponent $c$ |
|---|---|---|---|---|---|---|
| **T150-S75** | 18 | −1 | 7.21 | −0.063 | 0.34 | −0.14 |
| | | | $\epsilon_{ar} = \frac{7.21-\sigma_m}{18}\left(2N_f\right)^{-0.063} + 0.34\left(2N_f\right)^{-0.14}$ | | | |
| **T150-S100** | 15 | −1 | 6.1 | −0.074 | 0.32 | −0.089 |
| | | | $\epsilon_{ar} = \frac{6.1-\sigma_m}{15}\left(2N_f\right)^{-0.074} + 0.32\left(2N_f\right)^{-0.089}$ | | | |
| **T100-S75** | 12.5 | −1 | 5.0 | −0.075 | 0.15 | −0.06 |
| | | | $\epsilon_{ar} = \frac{5-\sigma_m}{12.5}\left(2N_f\right)^{-0.075} + 0.15\left(2N_f\right)^{-0.06}$ | | | |
| **T100-S100** | 12.5 | −1 | 2.8 | −0.091 | 0.10 | −0.192 |
| | | | $\epsilon_{ar} = \frac{2.8-\sigma_m}{12.5}\left(2N_f\right)^{-0.091} + 0.1\left(2N_f\right)^{-0.192}$ | | | |

As explained in Sect. 3.3, the modulus of elasticity is inversely proportional to textile comfort. Modulus is a measure of a material's stiffness or resistance to deformation, whereas compliance (comparable to textile comfort) is a measure of a material's ability to deform before fracturing. Materials with a high modulus value are generally stiff and brittle such as polystyrene and plexiglass. In contrast, materials with a low modulus value are generally more flexible and ductile. They require less stress to cause deformation and are more likely to deform significantly before fracturing [89]. Therefore, the inverse modulus and stretchability were compared to the previously reported works [9, 16, 32, 48–50, 80, 90–93] to highlight the importance of this work when selecting materials for specific applications. As illustrated in the results, the aerogel fibers fabricated in this study exhibit comparable or superior properties to those reported in previous work. This is attributed to the optimized gel spinning process and material composition. Overall, these Ashby charts (Fig. 8a and b) indicate that nanofibril mTPU is highly effective in enhancing the elongation at break and textile comfort. The results suggest that generating rubbery nanofibril in rigid aerogels is a promising area for future research.
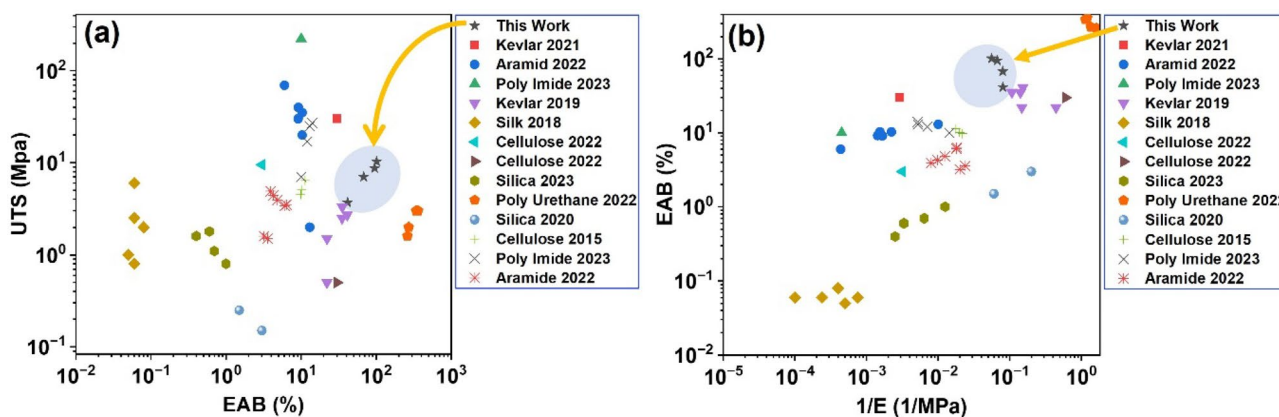


**Fig. 8** Ashby plots for comparing the results with previous works, showing **a** the ultimate tensile strength (UTS) against elongation at break (EAB) and **b** the elongation at break (EAB) versus inverse modulus (1/E)

# 4 Conclusion

In this study, highly viscous mTPU-SA pastes were converted into aerogel fibers through gel spinning processing. The nature of spinning procedure, flow-assisted stress-induced orientation, and crystallization concluded in thermally and mechanically robust aerogel fibers with dynamic reliability in fatigue experiments. The results confirmed the development of oriented nanofibrous mTPU during the gel spinning process.

Rheological investigation showed that the presence of SA particles enhances the strength and spinnability of mTPU solutions. Morphological, thermal, and mechanical analyses were conducted to investigate the structure and characteristics of samples with varying concentrations of the starting materials. The unique structure of hybrid mTPU-SA resulted in resilient and structurally stable aerogel fibers with tensile strength and elongation at break values of 10.26 MPa and 100.94%, respectively. Additionally, the incorporation of SA into the structure allowed us to achieve optimal thermal conductivity values ranging from 0.024 to 0.062 $W \cdot m^{-1} \cdot k^{-1}$, due to the uniform network and mesoporous structure. The superior thermal stability of mTPU-SA can be attributed to the presence of Si-O-Si bonds in the backbone.

This novel structure combines the eco-friendliness, biocompatibility, and biodegradability of base materials with the characteristics of aerogel materials such as low density, high specific surface area, and high porosity. As a result, this environmentally friendly nanoporous material exhibited satisfactory characteristics comparable to commercial products and can be extensively used in sustainable thermal insulation and biomedical applications where load-bearing properties are essential.

**Supplementary Information** The online version contains supplementary material available at https://doi.org/10.1007/s42114-024-00911-9.

**Author contribution** The manuscript was written with contributions from all authors. Hosseinali Omranpour: conceptualization, investigation, formal analysis, writing—original draft preparation, project administration; Soran Hassanifard: fatigue characterization; Ali Reza Monfared: processing and sample preparation; Babak O. Shahreza: morphological analysis; Amirmehdi Salehi: XRD and DMA analysis; Amirjalal Jalali: rheological investigation; Mohamad Kheradmandkeymousi: mechanical characterization; Saadman Sakib Rahman: SAXS and WAXS characterization; Kamran Behdinan: supervision, review and editing; Chul B. Park: conceptualization, supervision, funding acquisition, review and editing. All authors have approved the final version of the manuscript.

**Data availability** No datasets were generated or analysed during the current study.

## Declarations

**Conflict of interest** The authors declare no competing interests.

## References

1. Stanković SB, Popović D, Poparić GB (2008) Thermal properties of textile fabrics made of natural and regenerated cellulose fibers. Polym Test 27:41–48. https://doi.org/10.1016/J.POLYMERTESTING.2007.08.003

2. Fisher CH (2006) History of natural fibers. J Macromolecular Science: Part - Chem 15:1345–1375. https://doi.org/10.1080/00222338108056788

3. Chen YS, Fan J, Zhang W (2003) Clothing thermal insulation during sweating. Text Res J 73:152–157. https://doi.org/10.1177/004051750307300210

4. Fu M, Weng WG, Yuan HY (2014) Quantitative assessment of the relationship between radiant heat exposure and protective performance of multilayer thermal protective clothing during dry and wet conditions. J Hazard Mater 276:383–392. https://doi.org/10.1016/j.jhazmat.2014.05.056

5. Mandal S, Mazumder N-U-S, Agnew RJ, Song G, Li R (2021) Characterization and modeling of thermal protective and thermo-physiological comfort performance of polymeric textile materials-a review characterization and modeling of thermal protective and thermo-physiological comfort. Materials. https://doi.org/10.3390/ma14092397

6. Hao L, Yu W (2011) Comparison of thermal protective performance of aluminized fabrics of basalt fiber and glass fiber. Fire Mater 35:553–560. https://doi.org/10.1002/fam.1073

7. Kaufman WC, Bothe D (1979) Meyer SD (1982) Thermal insulating capabilities of outdoor clothing materials. Science 215:690–691. https://doi.org/10.1126/SCIENCE.215.4533.690

8. Wu C, Zeng L, Chang G, Zhou Y, Yan K, Xie L, Xue B, Zheng Q (2023) Composite phase change materials embedded into cellulose/polyacrylamide/graphene nanosheets/silver nanowire hybrid aerogels simultaneously with effective thermal management and anisotropic electromagnetic interference shielding. Adv Compos Hybrid Mater 6:31. https://doi.org/10.1007/s42114-022-00618-9

9. Li Q, Yuan Z, Zhang C, Hu S, Chen Z, Wu Y, Chen P, Qi H, Ye D (2022) Tough, highly oriented, super thermal insulating regenerated all-cellulose sponge-aerogel fibers integrating a graded aligned nanostructure. Nano Lett 22:3516–3524. https://doi.org/10.1021/acs.nanolett.1c03943

10. Kundu CK, Song L, Hu Y (2020) Sol-gel coatings from DOPO-alkoxysilanes: efficacy in fire protection of polyamide 66 textiles. Eur Polym J 125:109483. https://doi.org/10.1016/J.EURPOLYMJ.2020.109483

11. Yu Z, Liu J, Suryawanshi A, He H, Wang Y, Zhao Y (2021) Thermal insulating and fire-retarding behavior of treated cotton fabrics with a novel high water-retaining hydrogel used in thermal protective clothing. Cellulose 28:2581–2597. https://doi.org/10.1007/s10570-021-03696-y

12. Paul HL, Diller KR (2003) Comparison of thermal insulation performance of fibrous materials for the advanced space suit. J Biomech Eng 125:639–647. https://doi.org/10.1115/1.1611885

13. Han GC, Kumar S (2008) Materials science: making strong fibers. Science (1979) 319:908–909. https://doi.org/10.1126/science.1153911

14. Kim ES, Park HE, Lee PC (2018) In situ shrinking fibers enhance strain hardening and foamability of linear polymers. Polym (Guildf) 136:1–5. https://doi.org/10.1016/J.POLYMER.2017.12.040

15. Yokohara T, Nobukawa S, Yamaguchi M (2011) Rheological properties of polymer composites with flexible fine fibers. J Rheol (N Y N Y) 55:1205–1218. https://doi.org/10.1122/1.3626414

16. Du Y, Zhang X, Wang J, Liu Z, Zhang K, Ji X, You Y, Zhang X (2020) Reaction-spun transparent silica aerogel fibers. ACS Nano 14:11919–11928. https://doi.org/10.1021/acsnano.0c05016

17. Tafreshi OA, Mosanenzadeh SG, Karamikamkar S, Saadatnia Z, Park CB, Naguib HE (2022) A review on multifunctional aerogel fibers: processing, fabrication, functionalization, and applications. Mater Today Chem 23:100736

18. Li Y, Zhang X (2022) Electrically conductive, optically responsive, and highly orientated Ti3C2Tx MXene aerogel fibers. Adv Funct Mater 32:2107767. https://doi.org/10.1002/ADFM.202107767

19. He H, Liu J, Wang Y, Zhao Y, Qin Y, Zhu Z, Yu Z, Wang J (2022) An ultralight self-powered fire alarm e-textile based on conductive aerogel fiber with repeatable temperature monitoring performance used in firefighting clothing. ACS Nano 16:2953–2967. https://doi.org/10.1021/acsnano.1c10144

20. Kim GS, Hyun SH (2003) Effect of mixing on thermal and mechanical properties of aerogel-PVB composites. J Mater Sci 38:1961–1966. https://doi.org/10.1023/A:1023560601911

21. Wang X, Zhang Z, Wang Y, Malfait WJ, Zhao S, Tian Y, Liu T, Zhang X, Du A, Shen J (2023) Flexible, high-temperature-resistant silica-polymer aerogel hybrids by templating poly-methylsilsesquioxane microstructure with trace polyimide. Adv Compos Hybrid Mater 6:1–14. https://doi.org/10.1007/s42114-022-00587-z

22. Karamikamkar S, Naguib HE, Park CB (2020) Advances in precursor system for silica-based aerogel production toward improved mechanical properties, customized morphology, and multifunctionality: a review. Adv Colloid Interface Sci 276:102101. https://doi.org/10.1016/J.CIS.2020.102101

23. Afroze JD, Tong L, Abden MJ, Chen Y (2023) Multifunctional hierarchical graphene-carbon fiber hybrid aerogels for strain sensing and energy storage. Adv Compos Hybrid Mater 6:1–13. https://doi.org/10.1007/s42114-022-00594-0

24. Li M, Chen X, Li X, Dong J, Zhao X, Zhang Q (2022) Controllable strong and ultralight aramid nanofiber-based aerogel fibers for thermal insulation applications. Adv Fiber Mater 4:1267–1277. https://doi.org/10.1007/S42765-022-00175-2

25. Liu Z, Lyu J, Ding Y, Bao Y, Sheng Z, Shi N, Zhang X (2022) Nanoscale Kevlar liquid crystal aerogel fibers. ACS Nano 16:15237–15248. https://doi.org/10.1021/acsnano.2c06591

26. Monfared AR, Rezaei S, Rahman SS, Nakamura Y, Zaoui A, Omranpour H, Lee PC, Park CB (2024) Unleashing the power of SAN: innovative in situ fibrillation and moisture-crosslinking techniques yield stronger, tougher, and greener material than ABS. Compos B Eng 268:111103. https://doi.org/10.1016/J.COMPOSITESB.2023.111103

27. Smith P, Lemstra PJ (1980) Ultra-high-strength polyethylene filaments by solution spinning/drawing. J Mater Sci 15:505–514. https://doi.org/10.1007/BF02396802

28. Koziol K, Vilatela J, Moisala A, Motta M, Cunniff P, Sennett M, Windle A (2007) Windle A High-performance carbon nanotube fiber. Science (1979) 318:1892–1895. https://doi.org/10.1126/science.1147635

29. Linhares T, de Amorim MTP, Durães L (2019) Silica aerogel composites with embedded fibres: a review on their preparation, properties and applications. J Mater Chem Mater 7:22768–22802. https://doi.org/10.1039/C9TA04811A

30. Rezaei S, Zolali AM, Jalali A, Park CB (2021) Strong, highly hydrophobic, transparent, and super-insulative polyorganosiloxane-based aerogel. Chem Eng J 413:127488. https://doi.org/10.1016/j.cej.2020.127488

31. Rezaei S, Omranpour H, Rejeb Z, Ben, Fashandi M, Monfared AR, Rahmati R, Rastegardoost MM, Naguib HE, Park CB (2023) Super-hydrophobic and resilient hybrid silica aerogels for thermal

32. Liu Z, Lyu J, Fang D, Zhang X (2019) Nanofibrous Kevlar aerogel threads for thermal insulation in harsh environments. ACS Nano 13:5703–5711. https://doi.org/10.1021/acsnano.9b01094

33. Wang Z, Liu X, Macosko CW, Bates FS (2016) Nanofibers from water-extractable melt-blown immiscible polymer blends. Polym (Guildf) 101:269–273. https://doi.org/10.1016/J.POLYMER.2016.08.058

34. Cui Z, Marcelle S, Zhao M, Wu J, Liu X, Si J, Wang Q (2022) Thermoplastic polyurethane/titania/polydopamine (TPU/TiO2 / PDA) 3-D porous composite foam with outstanding oil/water separation performance and photocatalytic dye degradation. Adv Compos Hybrid Mater 5:2801–2816. https://doi.org/10.1007/S42114-022-00503-5

35. Zhao J, Wang G, Zhang A, Zhao G, Park CB (2021) Nanocellular TPU composite foams achieved by stretch-assisted microcellular foaming with low-pressure gaseous CO2 as blowing agent. J CO2 Utilization 53:101708. https://doi.org/10.1016/J.JCOU.2021.101708

36. Wang G, Wan G, Chai J, Li B, Zhao G, Mu Y, Park CB (2019) Structure-tunable thermoplastic polyurethane foams fabricated by supercritical carbon dioxide foaming and their compressive mechanical properties. J Supercrit Fluids 149:127–137. https://doi.org/10.1016/J.SUPFLU.2019.04.004

37. Menshutina N, Abramov A, Tsygankov P, Lovskaya D (2021) Extrusion-based 3D printing for highly porous alginate materials production. Gels 7:92–104. https://doi.org/10.3390/gels7030092

38. Tabernero A, Baldino L, Misol A, Cardea S, del Valle EMM (2020) Role of rheological properties on physical chitosan aerogels obtained by supercritical drying. Carbohydr Polym 233:115850. https://doi.org/10.1016/j.carbpol.2020.115850

39. Zhao S, Siqueira G, Drdova S, Norris D, Ubert C, Bonnin A, Galmarini S, Ganobjak M, Pan Z, Brunner S (2020) Additive manufacturing of silica aerogels. Nature 584:387–392. https://doi.org/10.1038/s41586-020-2594-0

40. Karamikamkar S, Abidli A, Behzadfar E, Rezaei S, Naguib HE, Park CB (2019) The effect of graphene-nanoplatelets on gelation and structural integrity of a polyvinyltrimethoxysilane-based aerogel. RSC Adv 9:11503–11520. https://doi.org/10.1039/C9RA00994A

41. Salgado M, Santos F, Rodríguez-Rojo S, Reis RL, Duarte ARC, Cocero MJ (2017) Development of barley and yeast β-glucan aerogels for drug delivery by supercritical fluids. J CO2 Utilization 22:262–269. https://doi.org/10.1016/J.JCOU.2017.10.006

42. Behera A (2022) Advanced materials: an introduction to modern materials science, 1st edn. Springer Cham

43. Tosh SM, Wood PJ, Wang Q, Weisz J (2004) Structural characteristics and rheological properties of partially hydrolyzed oat β-glucan: the effects of molecular weight and hydrolysis method. Carbohydr Polym 55:425–436. https://doi.org/10.1016/J.CARBPOL.2003.11.004

44. Argüelles-Monal W, Goycoolea PM, Peniche C, Higuera-Ciapara I (1998) Rheological study of the chitosan/glutaraldehyde chemical gel system. Polym Gels Networks 6:429–440. https://doi.org/10.1016/S0966-7822(98)00032-X

45. Carlos Fernández-Toledano J, Rodríguez J, Fern Andez-Toledano JC, Rodr Iguez -L, Opez J, Shahrivar K, Hidalgo-Alvarez R, Elvira L, De Montero F, De Vicente J (2014) Two-step yielding in magnetorheology. J Rheol (N Y N Y) 58:1507–1534. https://doi.org/10.1122/1.4880675

46. Compton BG, Lewis JA (2014) 3D printing: 3D-printing of light-weight cellular composites. Adv Mater 26:5930–5935. https://doi.org/10.1002/adma.201401804

47. Brummer Y, Defelice C, Wu Y, Kwong M, Wood PJ, Tosh SM (2014) Textural and rheological properties of oat beta-glucan gels

insulation, energy harvesting, and electrical applications in harsh environments. J Mater Chem C Mater 11:15106–15118. https://doi.org/10.1039/D3TC02862C

with varying molecular weight composition. J Agric Food Chem 62:3160–3167. https://doi.org/10.1021/JF405131D

48. Yin S, Zhang X, Hu G, Huang T, Yu H, Yu B, Zhu M (2022) In situ crosslinking of mechanically robust waterproof and moisture permeable cellulose diacetate nanofiber aerogels for warm clothing. Chem Eng J. https://doi.org/10.1016/j.cej.2022.136528

49. Bao Y, Lyu J, Liu Z, Ding Y, Zhang X (2021) Bending stiffness-directed fabricating of Kevlar aerogel-confined organic phase-change fibers. ACS Nano 15:15180–15190. https://doi.org/10.1021/ACSNANO.1C05693

50. Zhou W, Gong X, Li Y, Si Y, Zhang S, Yu J, Ding B (2022) Environmentally friendly waterborne polyurethane nanofibrous membranes by emulsion electrospinning for waterproof and breathable textiles. Chem Eng J 427:130925. https://doi.org/10.1016/J.CEJ.2021.130925

51. Omranpour H, Motahari S (2013) Effects of processing conditions on silica aerogel during aging: role of solvent, time and temperature. J Non Cryst Solids 379:7–11. https://doi.org/10.1016/j.jnoncrysol.2013.07.025

52. Yang J, Cao Q, Li Y, Li N, Qian H, Liu T, Wang M, Zhang X, Zhu X, Jiang B (2022) Multifunctional polysiloxane with high organic-to-inorganic conversion by the fast autocatalytic curing system. Ind Eng Chem Res 61:16023–16033. https://doi.org/10.1021/ACS.IECR.2C02763

53. Ederer J, Janoš P, Ecorchard P, Tolasz J, Štengl V, Beneš H, Perchacz M, Pop-Georgievski O (2017) Determination of amino groups on functionalized graphene oxide for polyurethane nanomaterials: XPS quantitation vs. functional speciation. RSC Adv 7:12464–12473. https://doi.org/10.1039/C6RA28745J

54. Ren F, Zhou R, Sun F, Ma H, Zhou Z, Xu W (2017) Blocked isocyanate silane modified Al2O3/polyamide 6 thermally conductive and electrical insulation composites with outstanding mechanical properties. RSC Adv 7:29779–29785. https://doi.org/10.1039/C7RA04454B

55. Gurunathan T, Chung JS (2017) Synthesis of aminosilane crosslinked cationomeric waterborne polyurethane nanocomposites and its physicochemical properties. Colloids Surf Physicochem Eng Asp 522:124–132. https://doi.org/10.1016/J.COLSURFA.2017.02.061

56. Zhao S, Pang H, Li Z, Wang Z, Kang H, Zhang W, Zhang S, Li J, Li L (2021) Polyurethane as high-functionality crosslinker for constructing thermally driven dual-crosslinking plant protein adhesion system with integrated strength and ductility. Chem Eng J 422:130152. https://doi.org/10.1016/J.CEJ.2021.130152

57. Cámara-Torres M, Sinha R, Scopece P, Neubert T, Lachmann K, Patelli A, Mota C, Moroni L (2021) Tuning cell behavior on 3d scaffolds fabricated by atmospheric plasma-assisted additive manufacturing. ACS Appl Mater Interfaces 13:3631–3644. https://doi.org/10.1021/ACSAMI.0C19687

58. Mel'nik IV, Lyashenko OV, Zub YL, Chuiko AA, Cauzzi D, Predieri G (2004) Synthesis of alkoxysilanes as starting substances for preparation of new materials by the sol-gel procedure. Silanes with urea functional group. Russ J Gen Chem 74:1658–1664. https://doi.org/10.1007/S11176-005-0080-X

59. Jiang J, Bu G, Yin Y, Wang C (2022) Synthesis and application of aminosiloxane-modified cationic waterborne polyurethane as fixing agent for nylon fabric. J Appl Polym Sci 139:51994. https://doi.org/10.1002/APP.51994

60. Qu YX, Guo KY, Pan HT, Wu ZH, Guo BF, Feng XL, Kong TT, Zhang C, Zhang GD, Zhao L, Gong LX, Gao JF, Liu HL, Mao ZN, Tang LC (2022) Facile synthesis of mechanically flexible and super-hydrophobic silicone aerogels with tunable pore structure for efficient oil-water separation. Mater Today Chem 26:101068. https://doi.org/10.1016/J.MTCHEM.2022.101068

61. Guan LZ, Gao JF, Pei YB, Zhao L, Gong LX, Wan YJ, Zhou H, Zheng N, Du XS, Wu L, Bin, Jiang JX, Liu HY, Tang LC, Mai YW (2016) Silane bonded graphene aerogels with tunable functionality and reversible compressibility. Carbon N Y 107:573–582. https://doi.org/10.1016/J.CARBON.2016.06.022

62. Lin J, Chen H, Fei T, Liu C, Zhang J (2013) Highly transparent and thermally stable superhydrophobic coatings from the deposition of silica aerogels. Appl Surf Sci 273:776–786. https://doi.org/10.1016/J.APSUSC.2013.02.134

63. Dourbash A, Motahari S, Omranpour H (2014) Effect of water content on properties of one-step catalyzed silica aerogels via ambient pressure drying. J Non Cryst Solids 405:135–140. https://doi.org/10.1016/j.jnoncrysol.2014.09.013

64. Scimeca M, Bischetti S, Lamsira HK, Bonfiglio R, Bonanno E (2018) Energy dispersive X-ray (EDX) microanalysis: a powerful tool in biomedical research and diagnosis. Eur J Histochem 62:89–99. https://doi.org/10.4081/EJH.2018.2841

65. Zhang S, Wang Z, Hu Y, Ji H, Xiao Y, Wang J, Xu G, Ding F (2022) Ambient pressure drying to construct cellulose acetate/benzoxazine hybrid aerogels with flame retardancy, excellent thermal stability, and superior mechanical strength resistance to cryogenic temperature. Biomacromolecules 23:5056–5064. https://doi.org/10.1021/ACS.BIOMAC.2C00904

66. ISO 15901-2 2022 - Pore size distribution and porosity of solid materials by mercury porosimetry and gas adsorption — part 2: analysis of nanopores by gas adsorption. https://www.iso.org/standard/67586.html. Accessed 28 Sep 2023

67. Bardestani R, Patience GS, Kaliaguine S (2019) Experimental methods in chemical engineering: specific surface area and pore size distribution measurements—BET, BJH, and DFT. Can J Chem Eng 97:2781–2791. https://doi.org/10.1002/CJCE.23632

68. Zhu X, Zhang R, Rong S, Zhang L, Ma C (2021) A systematic preparation mechanism for directional regulation of pore structure in activated carbon including specific surface area and pore hierarchy. J Anal Appl Pyrol 158:105266. https://doi.org/10.1016/J.JAAP.2021.105266

69. Rutledge GC, Lowery JL, Pai CL (2009) Characterization by mercury porosimetry of nonwoven fiber media with deformation. J Eng Fiber Fabr 4:1–13. https://doi.org/10.1177/155892500900400301

70. Bai M, Xiao J, Gao Y, Ding T (2023) Pore structure characteristics and mechanical property of engineered cementitious composites (ECC) incorporating recycled sand. Constr Build Mater 408:133721. https://doi.org/10.1016/J.CONBUILDMAT.2023.133721

71. Maleki H, Montes S, Hayati-Roodbari N, Putz F, Huesing N (2018) Compressible, thermally insulating, and fire retardant aerogels through self-assembling silk fibroin biopolymers inside a silica structure - an approach towards 3D printing of aerogels. ACS Appl Mater Interfaces 10:22718–22730. https://doi.org/10.1021/ACSAMI.8B05856

72. Tan L, Su Q, Zhang S, Huang H (2015) Preparing thermoplastic polyurethane/thermoplastic starch with high mechanical and biodegradable properties. RSC Adv 5:80884–80892. https://doi.org/10.1039/C5RA09713D

73. Wang Y, Chen X, Zhu W, Huang X, Tang XZ, Yang J (2019) A comparison of thermoplastic polyurethane incorporated with graphene oxide and thermally reduced graphene oxide: reduction is not always necessary. J Appl Polym Sci 136:47745. https://doi.org/10.1002/APP.47745

74. Khonakdar HA, Morshedian J, Wagenknecht U, Jafari SH (2003) An investigation of chemical crosslinking effect on properties of high-density polyethylene. Polym (Guildf) 44:4301–4309. https://doi.org/10.1016/S0032-3861(03)00363-X

75. Eom Y, Kim SM, Lee M, Jeon H, Park J, Lee ES, Hwang SY, Park J, Oh DX (2021) Mechano-responsive hydrogen-bonding array of thermoplastic polyurethane elastomer captures both strength and self-healing. Nature Commun 12:1–11. https://doi.org/10.1038/s41467-021-20931-z

76. Que YH, Shi Y, Liu LZ, Wang YX, Wang CC, Zhang HC, Han XY (2021) The crystallisation, microphase separation and mechanical properties of the mixture of ether-based TPU with different ester-based TPUs. Polymers 13:3475. https://doi.org/10.3390/POLYM13203475

77. Xu JK, Zhang L, Li DL, Bao JB, Wang ZB (2020) Foaming of poly(3-hydroxybutyrate- co-3-hydroxyvalerate) with supercritical carbon dioxide: foaming performance and crystallization behavior. ACS Omega 5:9839–9845. https://doi.org/10.1021/ACSOMEGA.9B04501/ASSET/IMAGES/MEDIUM/AO9B04501_M004.GIF

78. Lan B, Li P, Yang Q, Gong P (2020) Dynamic self generation of hydrogen bonding and relaxation of polymer chain segment in stabilizing thermoplastic polyurethane microcellular foams. Mater Today Commun 24:101056. https://doi.org/10.1016/J.MTCOMM.2020.101056

79. Fredi G, Dorigato A, Pegoretti A (2020) Dynamic-mechanical response of carbon fiber laminates with a reactive thermoplastic resin containing phase change microcapsules. Mech Time Depend Mater 24:395–418. https://doi.org/10.1007/S11043-019-09427-Y

80. Cui Y, Gong H, Wang Y, Li D, Bai H (2018) A thermally insulating textile inspired by polar bear hair. Adv Mater 30:1706807. https://doi.org/10.1002/adma.201706807

81. Aegerter MA, Leventis N, Koebel MM (2011) Aerogels handbook. Springer Science & Business Media

82. Tkalec G, Kranvogl R, Perva Uzunalić A, Knez Ž, Novak Z (2016) Optimisation of critical parameters during alginate aerogels' production. J Non Cryst Solids 443:112–117. https://doi.org/10.1016/J.JNONCRYSOL.2016.04.014

83. Zhao X, Ruan K, Qiu H, Zhong X, Gu J (2023) Fatigue-resistant polyimide aerogels with hierarchical cellular structure for broadband frequency sound absorption and thermal insulation. Adv Compos Hybrid Mater 6:1–10. https://doi.org/10.1007/S42114-023-00747-9

84. Engelbrecht-Wiggans AE, Forster AL (2023) Analysis of strain correction procedures for single fiber tensile testing. Compos Part Appl Sci Manuf 167:107411. https://doi.org/10.1016/J.COMPOSITESA.2022.107411

85. Ziarati HB, Fasihi M, Omranpour H (2020) The effect of resin formulation on the cellular morphology and mechanical properties of phenolic foams. J Appl Polym Sci 137:48331. https://doi.org/10.1002/APP.48331

86. Łagoda T, Vantadori S, Głowacka K, Kurek M, Kluger K (2022) Using the Smith-Watson-Topper parameter and its modifications to calculate the fatigue life of metals: the state-of-the-art. Mater (Basel) 15:3481. https://doi.org/10.3390/MA15103481

87. Dowling NE (2013) Mechanical behavior of materials: Engineering methods for deformation, fracture, and fatigue, 4th edn. Pearson

88. Hassanifard S, Hashemi SM (2020) On the strain-life fatigue parameters of additive manufactured plastic materials through fused filament fabrication process. Addit Manuf 32:100973. https://doi.org/10.1016/J.ADDMA.2019.100973

89. Vila M, Cáceres D, Prieto C (2003) Mechanical properties of sputtered silicon nitride thin films. J Appl Phys 94:7868–7873. https://doi.org/10.1063/1.1626799

90. Karadagli I, Schulz B, Schestakow M, Milow B, Gries T, Ratke L (2015) Production of porous cellulose aerogel fibers by an extrusion process. J Supercrit Fluids 106:105–114

91. Liu Y, Robertson M, Qiang Z, Meng Z, Ye C, Zhu M (2022) Ambient drying route to aramid nanofiber aerogels with high mechanical properties for low- k dielectrics. ACS Appl Polym Mater. https://doi.org/10.1021/ACSAPM.2C01806/SUPPL_FILE/AP2C01806_SI_002.MP4

92. Zhang X, Xu N, Jiang Y, Liu H, Xu H, Han C, Wang B, Wang Y (2023) Robust, fire-resistant, and thermal-stable SiZrNOC nanofiber membranes with amorphous microstructure for high-temperature thermal superinsulation. J Adv Ceram 12:36–48. https://doi.org/10.26599/JAC.2023.9220664

93. Wang D, Peng Y, Dong J, Pu L, Chang K, Yan XP, Qian HL, Li L, Huang Y, Liu T (2023) Hierarchically porous polyimide aerogel fibers based on the confinement of Ti3C2Tx flakes for thermal insulation and fire retardancy. Compos Commun 37:101429. https://doi.org/10.1016/J.COCO.2022.101429